



## Analysis of the Illapel Mw = 8.3 Thrust Earthquake Rupture Zone Using GOCE-Derived Gradients

ORLANDO ÁLVAREZ,<sup>1,2</sup> AGUSTINA PESCE,<sup>1,2</sup> MARIO GIMENEZ,<sup>1,2</sup> ANDRES FOLGUERA,<sup>3</sup> SANTIAGO SOLER,<sup>4</sup> and WENJIN CHEN<sup>5,6</sup>

**Abstract**—Satellite gravimetry has proven to be a useful tool to identify mass anomalies along a subduction interface, interpreted as heterogeneities related to the rupture process during megathrust earthquakes. In the last years, different works, reinforced with data derived from satellite gravity missions as GRACE and now GOCE, have analyzed not only the static component of the Earth gravity field, but also its temporal variations and relation to the seismic cycle. In particular, during the last decade, the Chilean margin has been affected by three megathrust earthquakes (with Mw >8): Maule 2010 Mw = 8.8, Pisagua 2014 Mw = 8.2 and recently the Mw = 8.3 Illapel event. Then, the recently completed GOCE mission (November 2009 to November 2013) offered a unique opportunity to study the Maule February 2010 and Pisagua April 2014 events by means of gravity gradients, directly measured at satellite height altitudes, which allowed mapping density heterogeneities with greater detail than the gravity anomaly which has been used in most studies up to now. In the present work, we use the last GOCE model (GO\_CONS\_GCF\_2\_DIR\_R5), the one of higher spatial resolution ( $N = 300$ ,  $\lambda/2 \approx 66$  km) derived from satellite-only data. The methodology used is the same as that to study the previous events, with the addition that now we derived a relation between the associated depths of a causative mass with a determined degree of the spherical harmonic expansion. This allowed to “decompose” the

gravimetric signal, by cutting off the degree/order of the harmonic expansion, as depth increases. From this analysis, we found that prominent oceanic features such as the Challenger fracture zone and the Juan Fernandez ridge played a key role in latitudinal seismic segmentation for the Illapel earthquake rupture zone, acting as barriers/attenuators to the seismic energy release. We compared the slip model from Tilmann et al. (Geophysical Research Letters 43: 574–583, doi:10.1002/2015GL066963, 2016) for the Illapel earthquake with vertical gravity gradient with and without sediment correction, and at different degree/order of the harmonic expansion. From this analysis, we inferred that prominent oceanic features over the subducting Nazca plate play a key role in seismic segmentation not only at heavily sedimented trenches, but also at sediment-starved segments.

**Key words:** Vertical gravity gradient, Megathrust earthquakes, South central Andes, Spherical harmonics, GOCE.

### 1. Introduction

Rupture areas related to large subduction earthquakes have been studied by means of gravity since the pioneer works of Song and Simons (2003) and Wells et al. (2003), among others. Then the different variables governing this relationship have been analyzed by different authors (e.g., Llenos and Mc Guire 2007; Sobiesak et al. 2007; Tassara 2010; Maksymowicz et al. 2015; among others). Fuchs et al. (2013) observed coseismic gravity changes from the Japan Tohoku-Oki 2011 earthquake with GOCE (Gravity Field and Steady State Ocean Circulation Explorer) gravity gradiometry, concluding that these variations left a statistically significant signal in the GOCE-measured gravity gradients. This work indicated that it was possible to detect coseismic gravity changes by spaceborne gradiometry as GOCE. More recently, slip distribution for great megathrust earthquakes along the

---

This paper is part of the article collection on “Illapel, Chile, Earthquake on September 16th, 2015”.

<sup>1</sup> Instituto Geofísico Sismológico Ing. F.S. Volponi, Universidad Nacional de San Juan, Ruta 12, Km 17, Jardín de los Poetas, Marquesado, Rivadavia, San Juan, Argentina. E-mail: orlando\_a\_p@yahoo.com.ar; orlando.alvarez@conicet.gov.ar; pesce.agustina@gmail.com; gimmario@gmail.com

<sup>2</sup> Consejo Nacional de Investigaciones Científicas y Técnicas (CONICET), Buenos Aires, Argentina.

<sup>3</sup> Departamento de Cs, Geológicas, INDEAN, Instituto de Estudios Andinos “Don Pablo Groeber”, FCEN, Universidad de Buenos Aires, Buenos Aires, Argentina. E-mail: andresfolguera2@yahoo.com.ar

<sup>4</sup> Facultad de Ciencias Exactas, Ingeniería y Agrimensura, Universidad Nacional de Rosario, Rosario, Argentina. E-mail: santiago.r.soler@gmail.com

<sup>5</sup> School of Geodesy and Geomatics, Institute of Geodesy and Geophysics, Wuhan, China. E-mail: chenwenjinwhu@gmail.com

<sup>6</sup> Department of Mathematics and Geosciences, University of Trieste, Trieste, Italy.

Peru–Chile margin has been correlated to GOCE-derived vertical gravity gradients (Alvarez et al. 2014, 2015a). These works established a correspondence between the long wavelengths of GOCE-derived vertical gravity gradient and internal slip in a rupture zone, a relationship that reinforces as both slip and event magnitude increase. GOCE data allow the characterization of crustal structure along different plate boundaries, with the Peru–Chile margin being an exceptional case of study since it has been affected by several megathrust earthquakes with large rupture areas reaching hundreds of kilometers.

In particular, the Maule 2010  $M_w = 8.8$  event shows the better agreement between positive slip distribution and negative vertical gravity gradient lobes from GOCE (see Fig. 9a, “Appendix 1”). On the other hand, the case of Pisagua  $M_w = 8.2$  and Iquique  $M_w = 7.7$  2014 earthquakes are quite different from the previous case, since the trench is almost sediment starved with no negative vertical gravity gradient lobes (see Fig. 8a, “Appendix 1”). The Iquique sequence was preceded by intense foreshock activity and characterized as a slow slip event (Ruiz et al. 2014; Bürgmann 2014; Schurr et al. 2014; Moreno et al. 2014; Lay et al. 2014; Bedford et al. 2015; Cesca et al. 2016). This region with low sediment thickness and several subducted seamounts (Geersen et al. 2015) presents a positive gravity gradient signal from GOCE (Alvarez et al. 2015a). However, when comparing two subsequent GOCE models (GO\_CONS\_GCF\_2\_TIM\_R4 with an effective data volume of approximately 26.5 months from 01/11/2009 to 19/06/2012 and GO\_CONS\_GCF\_2\_TIM\_R5 with an effective data volume of approximately 42 months from 01/11/2009 to 21/10/2013, both obtained prior to event occurrence in April, 2014), a decreasing gravity appears (Fig. 1a) before these events (Alvarez et al. 2015a). This decrease in gravity matches the main rupture zones of both events, with the maximum slip area being limited to the north and south by positive values (see Fig. 8b, “Appendix 1”). Thus, gravity from GOCE would delineate accelerated mass transfer inland during the last stages of interseismic deformation before the rupture as determined by GPS measurements (Kendrick et al. 2001; Metois et al. 2013).

GOCE models (GO\_CONS\_GCF\_2\_TIM\_R4 and GO\_CONS\_GCF\_2\_TIM\_R5) cover a data span after the 2010  $M_w = 8.8$  Maule earthquake. The comparison

between both models reveals a gravity increase toward the coastline after the event, probably indicating uplift of the upper plate due to coseismic and post-seismic lithospheric stretching along the subduction zone (Figs. 1b, 9b, “Appendix 1”). In such a scenario, we have found a link between slip distribution in rupture zones and gravity-derived signal not only at highly sediment-filled trenches but also at sediment-starved ones.

The particular case of the  $M_w = 8.3$  Illapel earthquake occurred in a region with intermediate to low trench sediment infill (Ranero et al. 2006; Völker et al. 2006) (estimated thickness below 500 m). This event occurred on 16 September 2015, with varying preliminary estimated rupture areas (see Fig. 10, “Appendix 2”) from  $\sim 100 \text{ km} \times 100 \text{ km}$  (<https://www.csn.uchile.cl/estimacion-del-desplazamiento-que-produjo-el-terremoto-de-illapel-2015/>),  $\sim 150 \text{ km} \times 100 \text{ km}$  (<http://www.geol.tsukuba.ac.jp/~yagy/EQ/20150917/index.html>), up to  $\sim 250 \text{ km} \times 100 \text{ km}$  ([http://earthquake.usgs.gov/earthquakes/eventpage/us20003k7a-scientific\\_finitefault](http://earthquake.usgs.gov/earthquakes/eventpage/us20003k7a-scientific_finitefault) and <http://www.earthobservatory.sg/news/September-16-2015-chile-earthquake>). In this region, the Nazca plate subducts horizontally for more than 500 km beneath South America between  $27.5^\circ$  and  $33.5^\circ$ S. The southern part of the flat slab, between the Juan Fernández aseismic ridge (JFR) and the Challenger Fracture Zone (Fz) (Figs. 2, 3) was identified as a seismic gap based on the occurrence of previous great earthquakes that affected the interplate zone (e.g., in 1943 by  $M_w = 7.9$  (Abe 1981; Beck et al. 1998), in 1880  $M_s = 7.7$  and 1730  $M_s = 8.7$  (Kelleher 1972; Nishenko 1985; Beck et al. 1998), the 1918  $M_s = 7.6/7.9$  event (Centro Sismológico Nacional, Universidad de Chile), and the 1873  $M_s = 8.0/8.9$  (Montessus de Ballore 1912; Boletín del Servicio Simológico de Chile del año 1910, pg. 254).

In this work, we calculate the vertical gravity gradient from the last GOCE model GO\_CONS\_GCF\_2\_DIR\_R5 (Bruinsma et al. 2013), developed up to different degrees/orders of the harmonic expansion and corrected by topographic and sediment effects to be compared to available slip distribution (Tilmann et al. 2016). The main objective of this work is to link rupture extent to specific crustal structures (acting as seismic barriers) in the downgoing oceanic Nazca plate, such as Challenger Fz and Juan Fernandez Ridge. Since available

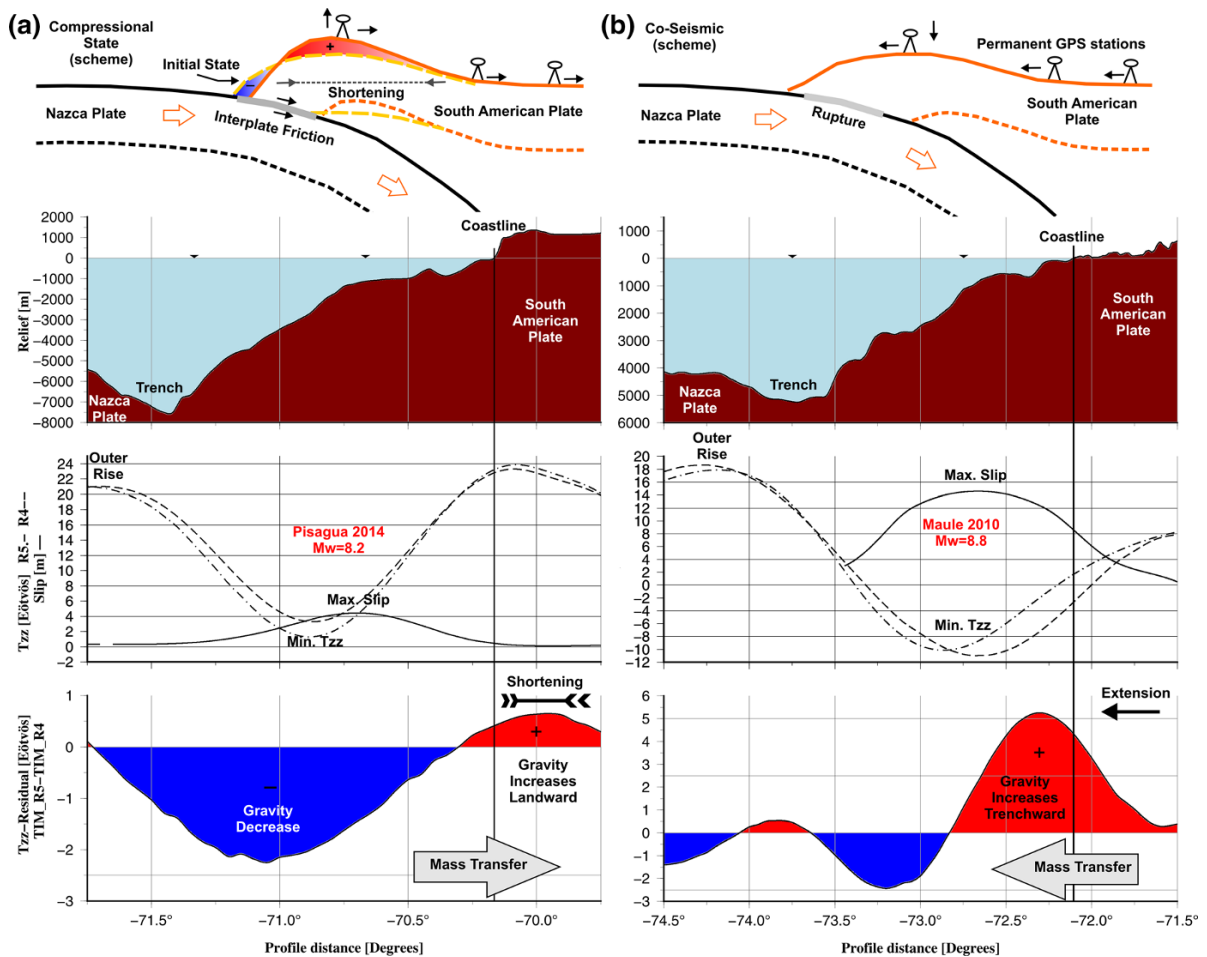


Figure 1

Gravity and the seismic cycle. **a** *Uppermost* Scheme indicating strain accumulation during the elastic compressional state when downgoing-subducted and *upper plates* are effectively coupled. Shortening and uplift in the *upper plate* forearc zone are indicated by GPS data. The difference between GOCE models GO\_CONS\_GCF\_2\_TIM\_R5 and GO\_CONS\_GCF\_2\_TIM\_R4 (*bottom*) is interpreted as mass transfer inland during this contractional stage for the Pisagua-Iquique 2014 sequence. **b** *Uppermost* coseismic stage showing the *upper plate* extension/relaxation during decoupling of the downgoing-subducted and *upper plates*, and oceanward mass transfer during and after earthquake occurrence (*bottom*) for the Maule 2010 earthquake. See Figs. 8b and 9b (“Appendix 1”) for a plan view and profiles location

seismic data might not be enough to delineate those structures, GOCE data (with homogeneous coverage) are used to define this relation with more precision. Additionally, we analyze the relationship between prominent oceanic features and trench sediment infill with seismic segmentation along this Central Chile margin.

## 2. Oceanic Features and Seismic Segmentation

The southern Pampean flat subduction zone coincides with the subduction of the Juan Fernández ridge,

an aseismic volcanic chain formed in a hot spot  $\sim 900$  km west of the Chilean trench. This feature would have collided first in the north ( $\sim 20^\circ$ ) at about 22 Ma and then migrated southward along the Chilean trench to its current collision point at about  $33.5^\circ\text{S}$ , due to an inferred broken geometry determined from conjugated aseismic ridges on the western Pacific floor, to the west of the Pacific mid-ocean ridge (Yáñez et al. 2001). The collision of the Juan Fernández ridge (Fig. 3) produced tectonic erosion, associated forearc extensional deformation (von Huene et al. 1997) and local uplift (Ranero et al. 2006). Additionally, this

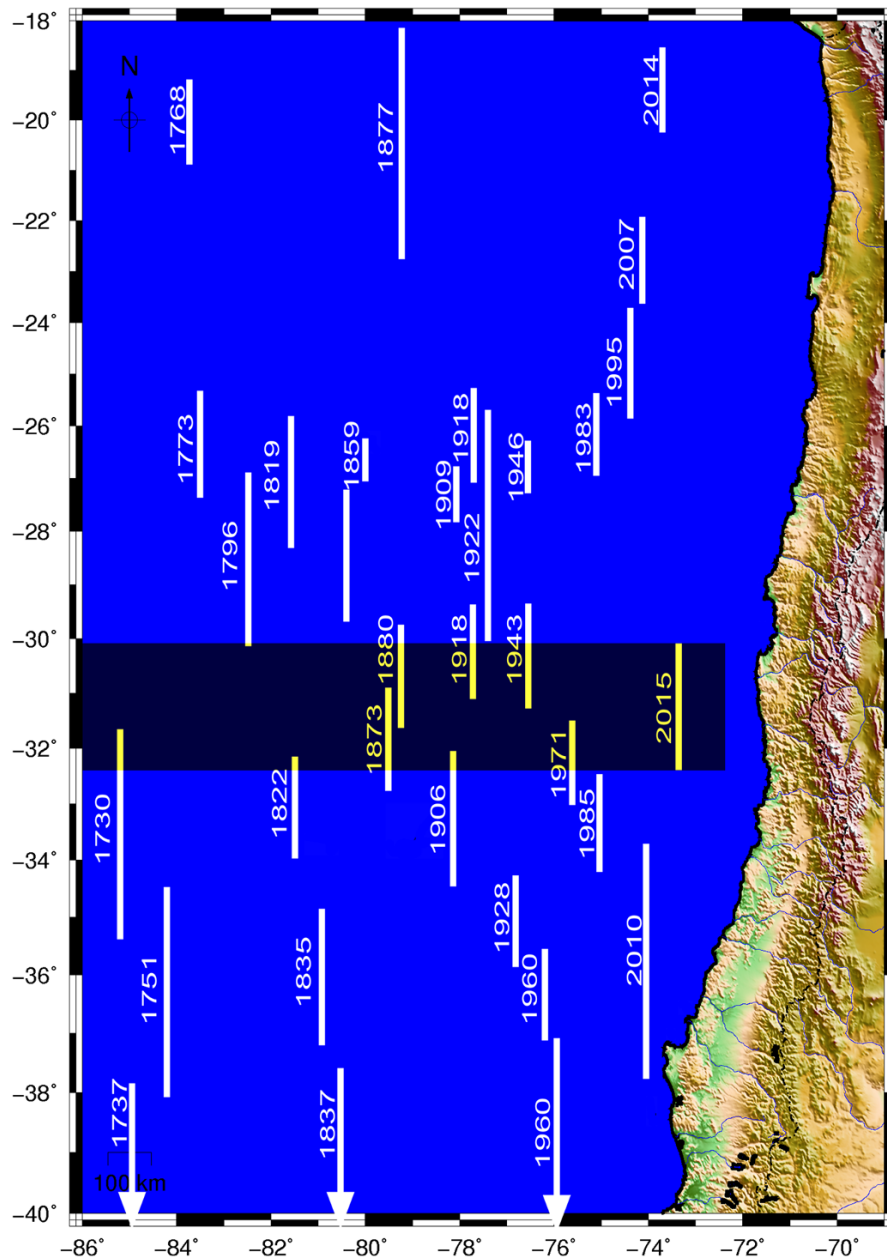


Figure 2

Updated historical great subduction earthquakes ruptures along the Peru–Chile margin from the eighteenth to twenty-first centuries (for more details see: Sparkes et al. 2010; Contreras-Reyes and Carrizo 2011, and references therein)

feature restrains the northward dispersion of sediments along the trench axis (Fig. 4) separating a heavily sedimented trench to the south (2.2–3.5 km) from a trench segment to the north that contains less than 1 km of stacked turbidic deposits confined to a narrow axial zone (Schweller et al. 1981; Bangs and Cande 1997;

Völker et al. 2006). Sediments over the Nazca plate show a substantial decrease north of the Challenger Fz, also acting as a topographic barrier to sediment distribution.

The subduction of high oceanic features, such as aseismic ridges, seamounts and fracture zones, has

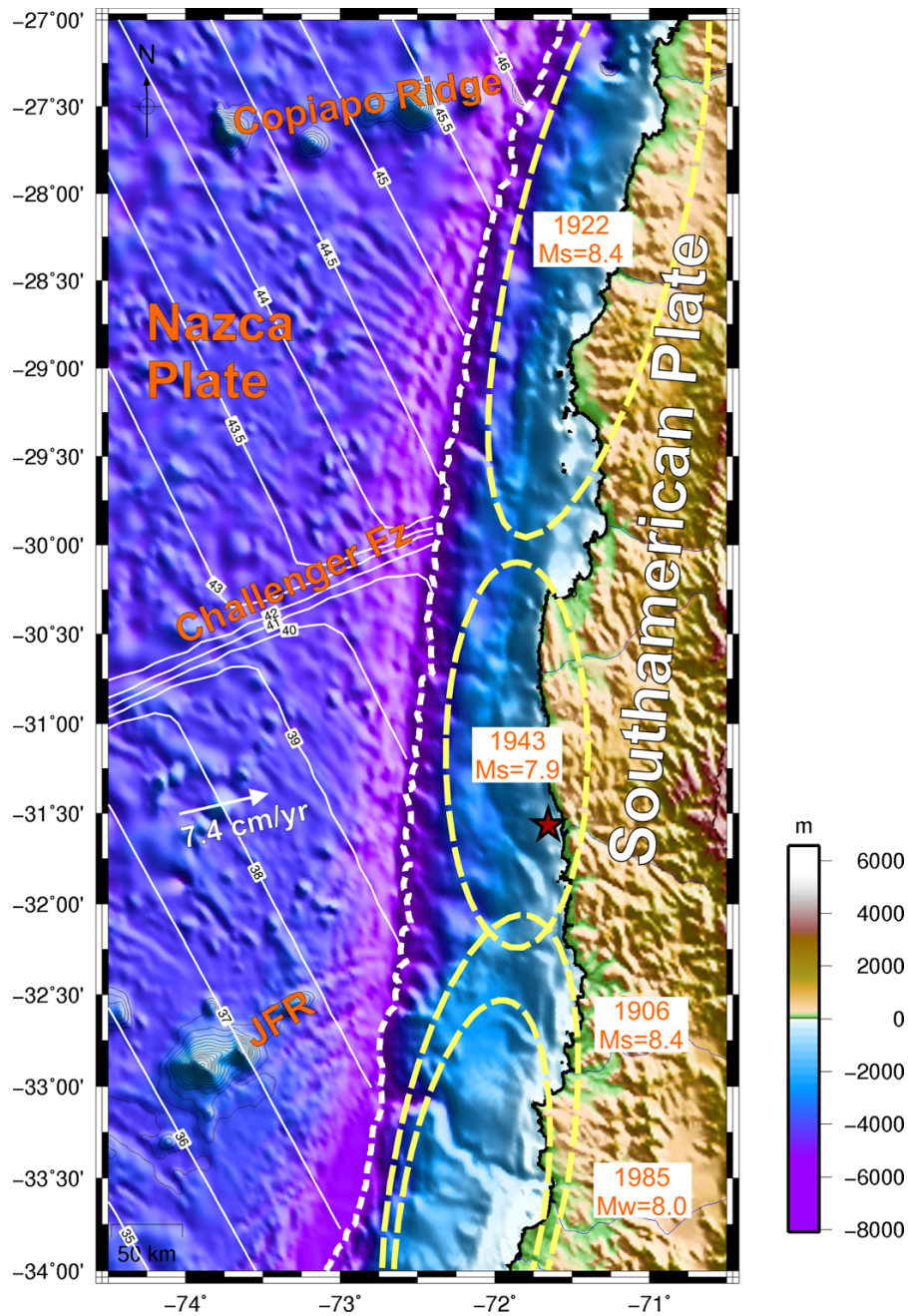


Figure 3

Nazca plate morphology (ETOPO1, Amante and Eakins 2009) highlighting the main bathymetric features such as the Juan Fernandez ridge, Challenger Fz and Copiapó ridge that are subducted beneath the South American plate. The differences in sediment thickness north and south of the Juan Fernandez ridge that marks a deep and shallow trench, respectively, are clearly depicted by the flat (smoothed) relief to the south of JFR. Nazca/South America convergence rate is approximately 7.4 cm/year with a convergence angle of 78°N (DeMets et al. 2010; Kendrick et al. 2003). *Solid white line* indicates plate ages (Müller et al. 2008); *black line* shows the coastline; *white dotted line* indicates the Chilean trench. Superimposed slip distributions of the main earthquakes (*yellow ellipses*): 1922 Ms = 8.3 (Beck et al. 1998); 1943 Mw = 7.9 (Abe 1981; Beck et al. 1998); 1985 Mw = 8.0 and 1906 Ms = 8.4 (Barrientos 1988, 1995; Mendoza et al. 1994; Beck et al. 1998; Comte et al. 1986; Christensen and Ruff 1986). *Red star* indicates the 2015 Mw = 8.2 Illapel earthquake epicenter

been related to deformational and morphological segmentation along the margin, which is in turn usually accompanied by seismic segmentation (Kelleher and Mc Cann 1976; Lay et al. 1982; Cloos 1992; Cloos and Shreve 1996; Scholz and Small 1997; Bilek 2007; Das and Watts 2009; Watts et al. 2010; Contreras-Reyes and Carrizo 2011; Müller and Landgrebe 2012; Sparkes et al. 2010; Landgrebe and Müller 2015). In particular, at heavily sedimented trenches, the relationship between sediment thickness and seafloor roughness appears to be of great influence in seismic segmentation. When high volumes of sediments are subducted, the subduction interface is smoothed, resulting in a homogenous plate interface. This allows seismic ruptures to overcome bathymetric barriers favouring trench-parallel propagation (Contreras-Reyes et al. 2010; Heuret et al. 2012; Ruff 1989; Schertwath et al. 2009; among others).

On September 16, 2015 at UTC time 22:54:32, an  $M_w = 8.3$  earthquake occurred offshore Chile, with epicenter location ( $31.570^\circ\text{S}$ ,  $71.654^\circ\text{W}$ ) near Illapel at an estimated depth of 25.0 km (USGS National Earthquake Information Center—NEIC: <http://earthquake.usgs.gov/earthquakes/>). GCMT (Global Centroid Moment Tensor) obtained a hypocenter location at  $31.22^\circ\text{S}$ ,  $72.27^\circ\text{W}$ , with a depth of approximately 17.8 km (<http://www.globalcmt.org/CMTsearch.html>). Fault geometry and location are consistent with the slip of the Nazca plate beneath the South American plate as indicated by seismic source parameters (e.g., [http://earthquake.usgs.gov/earthquakes/eventpage/us20003k7a#scientific\\_tensor:us\\_us\\_20003k7a\\_mwc\\_gemt](http://earthquake.usgs.gov/earthquakes/eventpage/us20003k7a#scientific_tensor:us_us_20003k7a_mwc_gemt) <http://ds.iris.edu/spud/momenttensor/10090604> <https://www.csn.uchile.cl/fase-w-terremoto-illapel-2015/>). Preliminary estimates indicated that the trench-parallel-rupture length reached up to 200–250 km over the plate boundary in the offshore region of Illapel from approximately  $30.25^\circ\text{S}$  to  $32.25^\circ\text{S}$ , with a maximum slip in the order of 9 m. On the other hand, the last big earthquake in this region had occurred on April 6, 1943 with an estimated magnitude of  $M_w = 7.9$  (Figs. 2, 3) presenting a similar rupture zone (Abe 1981; Beck et al. 1998). The region located north of  $30.25^\circ\text{S}$  had a ruptured  $\sim 450$  km zone along the trench through an  $M_s = 8.3$  earthquake on November 11, 1922 (Beck

et al. 1998). In contrast, the region between  $32^\circ\text{S}$  and  $34.5^\circ\text{S}$  located to the south of the Illapel earthquake (Figs. 2 and 3) presents a higher activity, recording recent large events as the July 9, 1971  $M_w = 7.8$ , the March 3 1985  $M_w = 8.0$  Valparaíso earthquakes, the August 17 1906  $M_s = 8.4$  big earthquake (Barrientos 1988, 1995; Mendoza et al. 1994; Beck et al. 1998; Comte et al. 1986; Christensen and Ruff 1986), and further south the February 27 2010  $M_w = 8.8$  Maule event.

Preliminary slip models for Illapel earthquake are quite different, since these are only based on teleseismic wave inversion, showing the occurrence of one ([http://earthquake.usgs.gov/earthquakes/eventpage/us20003k7a-scientific\\_finitefault](http://earthquake.usgs.gov/earthquakes/eventpage/us20003k7a-scientific_finitefault), <http://www.geol.tsukuba.ac.jp/~yagy/EQ/20150917/index.html>) or two main slip patches (<https://www.csn.uchile.cl/estimacion-del-desplazamiento-que-produjo-el-terremoto-de-illapel-2015/>, <http://www.earthobservatory.sg/news/September-16-2015-chile-earthquake>) with rupture sizes ranging from  $30^\circ\text{S}$  to  $32.5^\circ\text{S}$  (“Appendix 2”). Despite these differences, these models show a good agreement in the identification of the main slip located to the N–NW of the epicenter (See (“Appendix 2”, Fig. 10). In a recent work, Tilmann et al. (2016) derived a refined slip distribution (Fig. 5) by a joint inversion combining geodetic and seismological data sets (teleseismic, local waveform, strong-motion, high-rate GPS, GPS and InSAR data). They constrained the coseismic rupture process in detail based on these data sets, finding that the earthquake nucleated near the coast but then propagated northward and updip, with a maximum slip of 5–6 m.

### 3. Methodology

This methodology has already been used in Álvarez et al. (2014, 2015a, b, c), with a detailed description of it in Álvarez et al. (2012, 2013). We performed a direct modeling from satellite GOCE model GO\_CONS\_GCF\_2\_DIR\_R5 (Bruinsma et al. 2013). This is a satellite-only model based on a full combination of GOCE-SGG (Satellite Gravity Gradiometer) and GOCE-SST (Satellite-to-Satellite Tracking) that also incorporates GRACE (Gravity

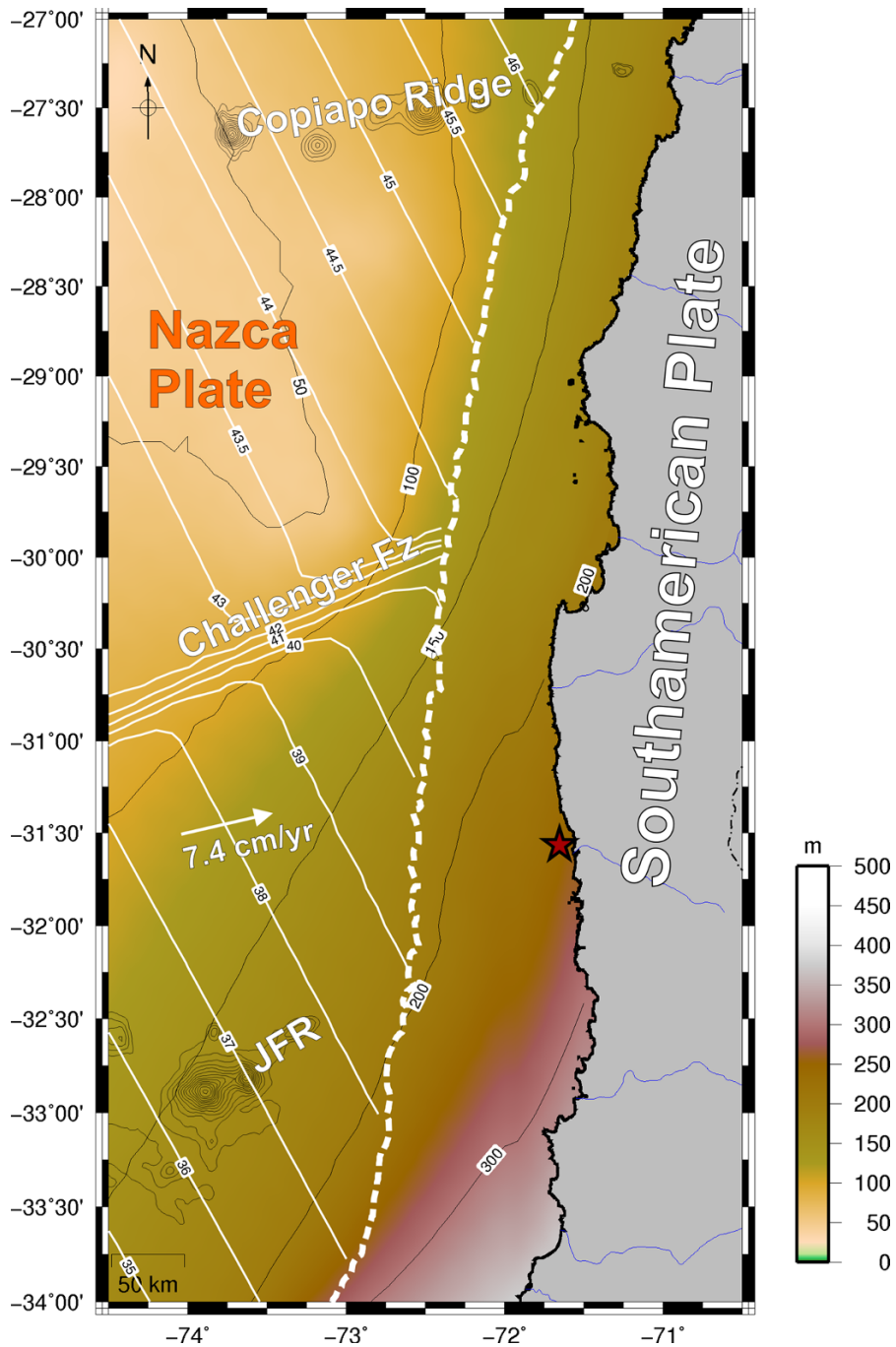


Figure 4

Sediment thickness distribution from Whittaker et al. (2013) corresponding to an updated version of Divins (2003). Differences in trench sediment thickness are related to the inception of the Juan Fernández ridge at the Chilean trench in the last 10 My at these latitudes, which acts as a topographic barrier restraining the northward sediment transport. Sediments over the Nazca plate also show a substantial decrease north of the Challenger Fz which also acts as a topographic barrier to sediment distribution. *Red star* indicates the 2015 Mw = 8.2 Illapel earthquake epicenter

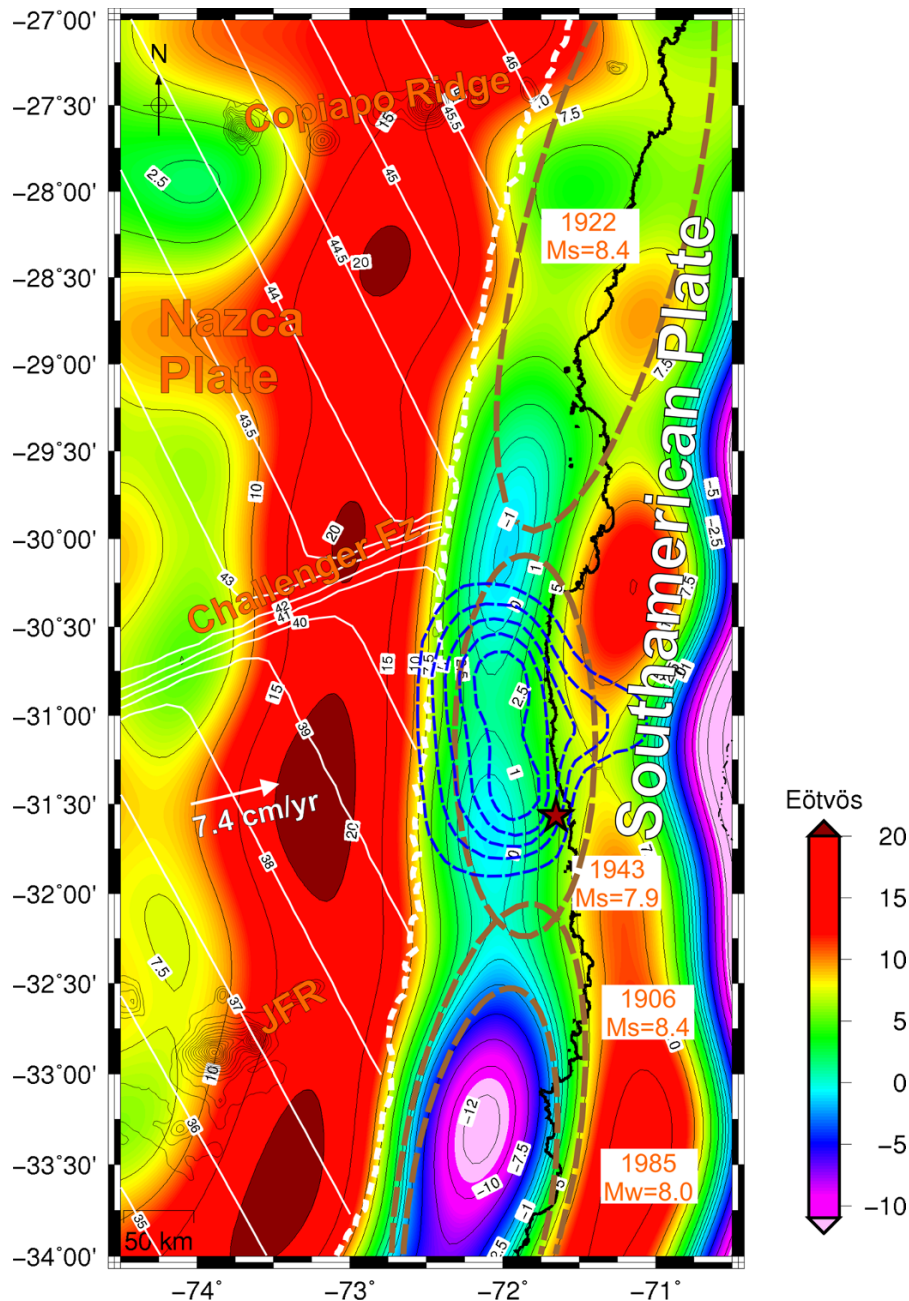


Figure 5

Topography- and sediment-corrected vertical gravity gradient in the South Central Andes and adjacent Nazca plate, obtained from GOCE satellite-only model GO\_CONS\_GCF\_2\_DIR\_R5 (Bruinsma et al. 2013). Ocean floor age (solid white lines), bathymetric highs (solid black contours over the Nazca plate) and main historical rupture zones are indicated (brown ellipses); for more detailed references see Fig. 3. Red star indicates the 2015  $M_w = 8.2$  Illapel earthquake epicenter and the blue dashed line the slip distribution from Tilmann et al. (2016)

Recovery and Climatic Experiment) and LAGEOS (LAser GEodynamics Satellite) data. This data combination leads to an excellent performance of the long as well as of the short wavelengths (processing

details are given in Pail et al. 2011; Bruinsma et al. 2010). The advantage of using a satellite-only model is that the quality of the data presents homogeneous precision, while models that include terrestrial data

(e.g., EGM2008/EIGEN, a spatially heterogeneous combination of data) present varying quality due to errors or sampling biases of the original terrestrial data (Braitenberg et al. 2011; Bomfim et al. 2013). This model was obtained by the direct approach method and is the one of maximum degree/order ( $N = 300$ ) from satellite-only data, with an effective data volume of approximately  $\sim 19380$  orbital revolutions (data period: 01/11/2009–20/10/2013, i.e.,  $\sim 3.45$  years). The half-wavelength resolution is of approximately 67 km according to  $\lambda/2 = \pi R/N_{\max}$  (Li 2001; Hofmann-Wellenhof and Moritz 2006; Barthelmes 2013), with  $R$  being the mean Earth radius and  $N_{\max}$  the maximum degree/order of the harmonic expansion.

We calculate the second derivative of the disturbing potential in the radial direction, or vertical gravity gradient (Tzz), from the spherical harmonic coefficients (Janak and Sprlak 2006) on a regular grid of 0.05 grid cell size. The Tzz is expressed in Eötvös ( $10^{-4}$  mGal/m) and, since it is a gravity derivative, it represents a better theoretical resolution than the gravity vector itself for some geophysical features (Li 2001), allowing to determine the location of anomalous masses with better detail and accuracy (Braitenberg et al. 2011).

To remove the topographic effect from the gravity derivative, we performed the topographic correction by discretizing a digital elevation model (ETOPO1, Amante and Eakins 2009) using spherical prisms of constant density (Heck and Seitz 2007; Wild-Pfeiffer 2008; Grombein et al. 2013; among others). In this way, using a spherical approximation instead of a planar one, we take into account the Earth's curvature (Uieda et al. 2010), avoiding considerable errors as the region under study is large enough (Braitenberg et al. 2011; Alvarez et al. 2012, 2013; Bouman et al. 2013; Grombein et al. 2013). We calculated the topography-generated Tzz from the digital elevation model (ETOPO1, Amante and Eakins 2009), using the software *Tesseroids* (Uieda et al. 2010; Alvarez et al. 2013). Adopted densities are mean standard values of  $2.67 \text{ g/cm}^3$  for masses above sea level and  $1.03 \text{ g/cm}^3$  for seawater. The selected calculation height is of 7000 m to ensure that all values are above the topography. The topographic correction amounts up to tens of Eötvös, with higher positive values over

the Andes and maximum negative values over the lowest topography such as the Peru–Chile trench (see Fig. 12a, “Appendix 4”).

The sediment correction was performed using the same method considering a mean density of  $2.4 \text{ g/cm}^3$  (see Fig. 12a, “Appendix 4”). Selected sediment densities were used in the region by Ranero et al. (2006) and obtained from modeling wide-angle seismic and gravity data (Sallares and Ranero 2005). Sediment thicknesses were obtained from NGDC's global ocean sediment thickness grid (Fig. 4) from Whittaker et al. (2013), an updated version of the NGDC's original ocean sediment thickness grid from Divins (2003).

#### 4. Results

The region comprehended between the sites of inception of the Copiapó and Juan Fernandez ridges into the Chilean trench is characterized by the sub-horizontal subduction of the Nazca plate known as Pampean flat slab (Cahill and Isacks 1992; Mulcahy et al. 2015; Alvarez et al. 2015b, among others). One of the main characteristics of the segment is a completely sediment-starved trench north of the Copiapó ridge and a heavily sedimented one south of the Juan Fernández ridge, with intermediate values between them (<500 m).

The topography- and sediment-corrected vertical gravity gradient (Fig. 5) shows a pronounced maximum positive at the outer rise region where the Nazca plate bends prior to subduction. This gravity high is segmented in the zone of inception of the Juan Fernández and Copiapó ridges (with higher buoyancy and compensating root), an anomaly that extends toward the coastline. While the subducted Copiapó ridge presents a positive value ( $+7.5$  Eötvös near the coast), the extrapolation of the Juan Fernández ridge beneath the South American Plate shows a narrowing of the signal (being positive or near-to-zero values). Seismic profiles (Von Huene et al. 1997) indicate a shallower oceanic crust next to the trench axis than elsewhere beneath the Juan Fernández ridge (Sandwell and Smith 1997), as expressed in the GA and Tzz maps (Alvarez et al. 2015a).

Relatively lower Tzz values along both ridge tracks are indicative of a thickened oceanic crust (as reported by von Huene et al. (1997) based on wide-angle seismic data for the Juan Fernández ridge). Sandwell and Smith (1997) had related negative satellite-derived gravity anomalies to a crustal root indicative of crustal flexure associated with seamount loading. Moho depths obtained from inversion of satellite GOCE-derived gravity data (Alvarez et al. 2015b) show maximum crustal thicknesses at the forearc zone, coincident with the inception of prominent oceanic features in the Chilean trench such as the Juan Fernández ridge, Challenger Fz, Copiapó and Taltal ridges.

South of the Juan Fernández ridge, extrapolation over the seismogenic zone (between the trench and the continental slope), the Tzz presents maximum negative values (less than  $-12$  Eötvös) coincidentally with the Valparaiso Basin (Alvarez et al. 2014). Negative Tzz values are related to sediment filling marginal sections and to sediment-filled deep sea terrace and slope basins resting upon thinned continental crust (ANCORP Working Group 2003; Flueh et al. 1998; von Huene et al. 1997; Wells et al. 2003; Alvarez et al. 2014), all of which have a lower density than the mean value used as reference ( $2.67$  g/cm<sup>3</sup>). As mentioned, the Juan Fernández ridge constitutes a topographic barrier within the trench that restrains the northward transport of these sediments along the axial channel (Yáñez et al. 2001). To the north of the Juan Fernández ridge, climatic conditions change (Lamb and Davis 2003) resulting in a less sedimented to a completely sediment-starved trench, where the Tzz signal exhibits a well-defined contour  $>+0$  Eötvös (Fig. 5), interpreted as indicative of this abrupt decrease in sediment fill (Fig. 4). Other authors (Bangs and Cande 1997; Von Huene et al. 1997; Ranero et al. 2006; Lohrmann et al. 2006; among others) had already reported  $<1$  km of sediment infill, confined to a narrow zone at the trench axis to the north of JFR. Differences in flexural behavior of the upper plate, north and south of the Juan Fernández ridge, were reported by Alvarez et al. (2015a), who found substantial variations in the crustal structure and flexural rigidity. To the north, over the southern part of the flat slab, plate rigidity becomes higher than in the southern zone where the

oceanic plate subducts at an approximately normal angle and upper plate rigidity falls near zero values (Alvarez et al. 2015b).

At the central part of the region under study, the Challenger Fz intercepts the Chilean trench producing extensive erosion along the continental slope ( $29.25^{\circ}\text{S}$  to  $30.25^{\circ}\text{S}$ ) (Yáñez et al. 2002). In this region over the plate interface, a negative lobe of Tzz is depicted (Fig. 5) probably related to sediment infill (see Figs. 4, 12b). In summary, the seismogenic zone between the Juan Fernández and Copiapó ridges presents a highly heterogeneous density structure as depicted by gravity data, with maximum negative values south of the Juan Fernández ridge (less than  $-12$  Eötvös), a lobe of low values north of it (near-to-zero Eötvös), a lobe of negative Tzz at the inception of the Challenger Fz (less than  $-1$  Eötvös) and a positive lobe (more than  $+5$  Eötvös) from these latitudes to the north up to the Copiapó ridge, where a maximum Tzz is observed.

## 5. Discussion

A heterogeneous density distribution along the rupture zone of the Illapel earthquake shown in the previous section and a mainly positive Tzz throughout it ( $>0$  Eötvös) (Fig. 5) preclude a direct correlation between negative Tzz values with high slips, as found for other events along the Peru–Chile margin (see Alvarez et al. 2014, 2015a). Such a correlation found in previous works suggests that Tzz is useful to delineate along the strike variable coupling of the seismogenic structure that occurs beneath the deep sea terrace and its basins.

While south of the point of inception of the Juan Fernández ridge into the trench, the rupture zones for the 1906 and 1985 earthquakes show good correlations with negative Tzz values, and the 1943 and 1922 rupture zones show no correlation at all with negative Tzz or relative Tzz minima (along this sediment-starved region, neither negative Tzz nor relative minima can be found to correlate with the rupture extent). Many authors agree that variable sediment thickness along the trench and the presence of high oceanic features control seismic segmentation, favoring trench-parallel rupture propagation at

heavily sedimented trenches (e.g., Ruff 1989; Lamb and Davis 2003; Schertwath et al. 2009; Contreras-Reyes et al. 2010; Contreras-Reyes and Carrizo 2011; Heuret et al. 2012; among others). This hypothesis can be supported by the relationship between minimum Tzz and maximum slip patches (at heavily sedimented segments of the margin).

In particular, Alvarez et al. (2014, 2015a) have shown a correlation between low Tzz lobes and high slip areas associated with the 1996 Mw = 7.7 Nazca, 2001 Mw = 8.4 Arequipa, 2007 Mw = 8.0 Pisco, 2010 Maule Mw = 8.8 and 1960 Valdivia Mw = 9.5 rupture zones, from the Patagonian trench to the Arica bend region, showing that the correlation between Tzz and slip increases as the event magnitude becomes higher. This relationship weakens at sediment-starved trench regions as in the case of the 2014 Mw = 8.2 Pisagua and 2014 Mw = 7.7 Iquique events, where Geersen et al. (2015) showed that lower plate irregularities, such as seamounts, most likely controlled interplate coupling and consequently seismic rupture.

As indicated, preliminary slip models for the Illapel event found a rupture length from approximately 30° to 32.5°S, with a maximum slip reaching 9 m N–NW of the epicenter (Fig. 10). The refined slip distribution from Tilmann et al. (2016) delineates a rupture length (blue dashed contours in Fig. 5) from approximately 30.25° to 31.9°S, with a maximum slip between 30.6°S and 31.6°S.

Our results (Fig. 5) show a narrowing in the Tzz signal between 32°S and 32.25°S, at the site of inception of the Juan Fernández ridge. At these latitudes, the prominent bathymetry of the subducted JFR causes an uplift of the trench and forearc topography, blocking axial sediment transport in the trench (Kopp 2013; Laursen et al. 2002; von Huene et al. 1997; Yáñez et al. 2001). Variations in sediment thickness along the trench and its relation to the incoming subducting high oceanic features strongly affect the development of the subduction channel and promote seismic segmentation (Contreras-Reyes and Carrizo 2011; Kopp 2013). The analysis of rupture lengths of historical great megathrust earthquakes in the region in addition to the above explained lead to consider that the JFR behaves as a seismic barrier in this region (e.g., Sparkes et al. 2010; Contreras-Reyes

and Carrizo 2011; Alvarez et al. 2014). Seismic segmentation hypothesis and seismic barriers that may control the seismic moment release and rupture areas have been proposed in several works (e.g., Kodaira et al. 2000; Bilek 2007; Sparkes et al. 2010; Scholl et al. 2010; Wang and Bilek 2011; Contreras-Reyes and Carrizo 2011; Müller and Landgrebe 2012; Heuret et al. 2012; among others). Based on a similar approach in a Tzz analysis, Alvarez et al. (2014) proposed that depending on the event magnitude, ruptures would cut across attenuators/barriers until the seismic energy was dissipated. In particular, for the Illapel event, the Juan Fernández ridge could have acted as an attenuator to the south of the rupture, while to the north the Challenger Fz could have blocked the rupture propagation.

Inland, rupture distribution contours (Tilmann et al. 2016) roughly coincide with a relative minimum of Tzz (Fig. 5), with the rupture being flanked north and south by higher Tzz values (more than +7.5 Eötvös). This is consistent with results presented in Alvarez et al. (2014) for the Constitución 2010 Mw = 7.0 (aftershock of Maule 2010, Ruiz et al. 2013) being the maximum slip between two Tzz highs. Similarly, the 1906 and 1985 ruptures ended to the east at a positive anomaly (more than +10 Eötvös) (see Fig. 5), which probably reveals the location of a seismic barrier marking the eastern edge of rupture propagation for the mentioned events.

The main slip peak for the Illapel earthquake is located between two Tzz lobes of relative minima (Fig. 5) and, as indicated, the relationship between high slips and low Tzz vanishes where the trench is sediment starved. A direct approach to analyze the influence of sediments over rupture propagation and their relation to gravity-derived signal is to calculate the Tzz with and without their effect. In this region, the effect of sediments is low (Fig. 12b) and consequently differences are smooth (Fig. 13). Additionally, we calculated Tzz up to different degree/order of the harmonic expansion to analyze the response as causative masses depth increase. Featherstone (1997) associated the depth ( $Z_1$ ) of a causative mass with a determined degree of the spherical harmonic expansion ( $N$ ) by performing a spectral analysis of the geoid and gravity anomalies. Here, we derived a similar equation, relating  $Z_1$  with a

determined  $N$  by performing an equivalent analysis for gravity anomalies and vertical gravity gradient (see “Appendix 5”):

$$Z_l = \frac{(R_E + H_C)(N - 1)}{(N + 2)(N + 1)},$$

where  $Z_l$  is the associated depth (for  $l = N$ ),  $R_E$  is the Earth’s radius,  $H_C$  is the Tzz calculation height and  $N$  is the selected degree/order of the harmonic expansion. While higher orders are associated with shallower sources (low  $Z_l$ ), decreasing orders are related to deeper structures (higher  $Z_l$ ). Table 1 (Appendix 5) shows the used degrees/orders, the corresponding depth  $Z_l$  and spatial resolution, using  $R_E = 6,371$  km as the mean Earth radius. This harmonic decomposition tool (by truncating the harmonic expansion) allows analyzing Tzz response with increasing depths of the causative masses (Fig. 6). Results combining different  $N$  and incorporating or not the sediment correction are presented in Fig. 13, to explore different alternatives of mass distribution and relationship to seismogenesis and rupture area. Results (Fig. 13) indicate that removing sediment effect is more relevant when calculating at higher degrees (related to shallower mass anomalies, Fig. 13a, b), while when calculating at lower degrees (related to deeper mass anomalies) sediment correction loses relevance (Fig. 13e, f).

The cutting off of the harmonic expansion degree from  $N = 300$  to  $N = 250$  (allowing to unveil deeper sources) resulted in a subtle migration of the Tzz

Figure 6  
Topography and sediment-corrected Tzz slices calculated at different degrees of the harmonic expansion. Degree orders between  $N = 225$  and  $300$  depict anomalies at approximate depths of the seismogenic zone (interplate contact), while higher degrees as  $N = 175$  and  $N = 150$  show the effect of the Juan Fernández ridge and Challenger Fz, respectively. In the right corner down the relief Moho depths from Alvarez et al. (2015c) are depicted

lobes toward the N–NE through the plate convergence direction (Fig. 13). The cutoff  $N = 225$  presents a Tzz lobe (2.5 Eötvös) in better agreement with the slip model from Tilmann et al. (2016). Inland, the Tzz anomalies show no significant variation, keeping a good correlation the isolines/isocurves with the relative minimum of Tzz. To the south of the extrapolation of the Juan Fernández ridge beneath the South American Plate, the minimum Tzz lobe suffers no major changes despite the different cutting off and removal of the sediment effect. For the Illapel earthquake, the best fit (between Tzz and slip distribution) is obtained without sediment correction and  $N$  between 225 and 250 (Fig. 13).

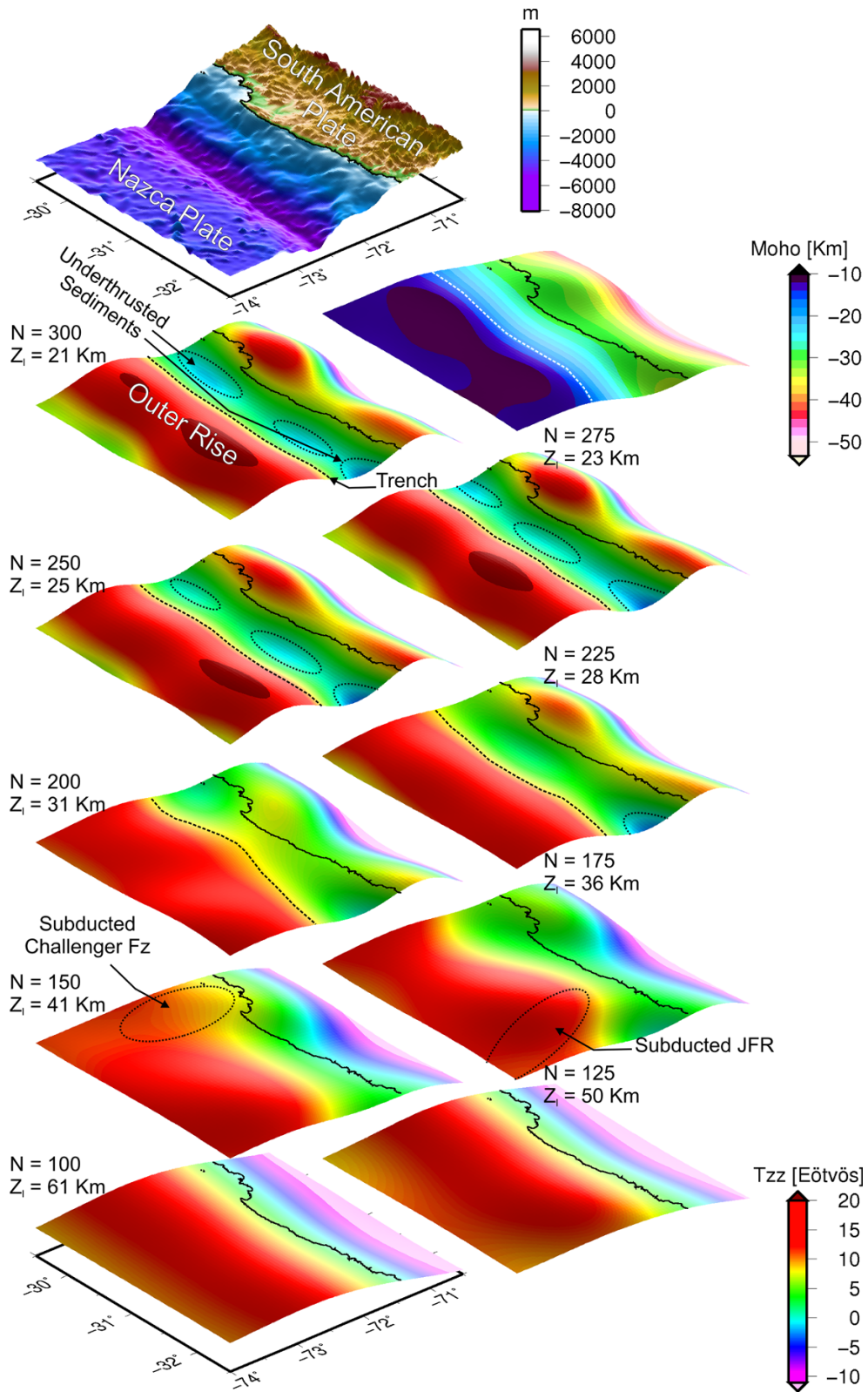
### 5.1. Oceanic features controlling rupture propagation

By cutting the harmonic expansion to lower degrees up to  $N = 100$ , we expand the limit of observation exploring at depth and analyzing deeper sources. Results indicate that the effect of the

Table 1

Associated depth ( $Z_l$ ) of a causative mass with a determined degree of the spherical harmonic expansion ( $N$ ) for geoid height and  $\Delta g$  (Featherstone 1997) and for our derived formulae for Tzz and  $\Delta g$

Degree/order $N$	Spatial resolution $\lambda/2 = \pi R/N_{\max}$ [Km]	$Z_l$ [Km] for $\Delta g$ (Eq. 6) (Featherstone 1997)	$Z_l$ [Km] for Tzz (Eq. 18) ( $H_C = 7$ km)
300	66.72	21.31	20.98
275	72.78	23.251	22.86
250	80.06	25.581	25.11
225	88.95	28.441	27.85
200	100.07	32.011	31.26
175	114.37	36.611	35.62
165	121.3	38.84	37.73
150	133.43	42.76	41.40
125	160.12	51.38	49.42
100	200.15	64.35	61.29



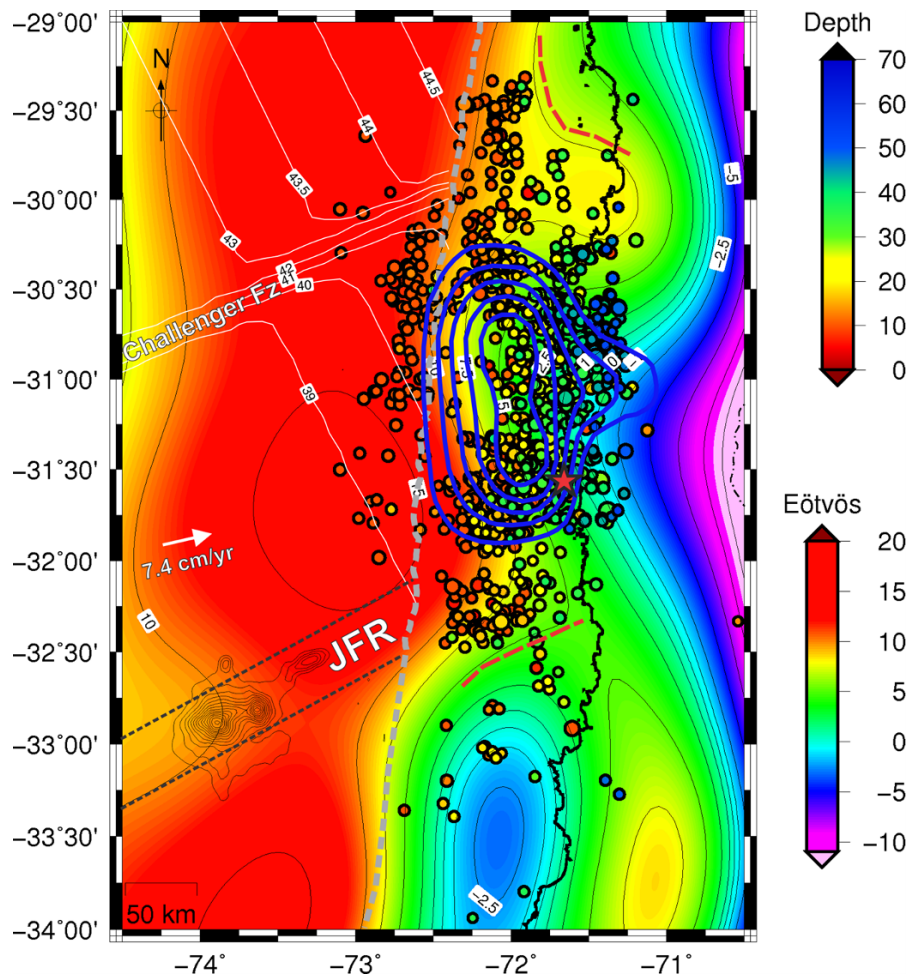


Figure 7

Topography and sediment-corrected vertical gravity gradient obtained from GOCE satellite-only model GO\_CONS\_GCF\_2\_DIR\_R5 (Bruinsma et al. 2013) up to  $N = 165$ . Ocean floor age (*solid white line*) marks the trend of the Challenger fracture zone. The Juan Fernandez ridge isolines are marked by *solid black contours*. *Red star* indicates the 2015  $M_w = 8.2$  Illapel earthquake epicenter and the *blue line* the slip distribution from Tilmann et al. (2016). The *orange dashed line* to the north follows the contour of a relative maximum Tzz that cuts across the seismogenic zone in coincidence with the extrapolated path of the subducted Challenger Fz. The *orange dashed line* to the south highlights the eastward inflection of the Tzz, mainly expressed by the  $+5\text{Eötvös}$  contour. This eastward inflection of the Tzz signal coincides with the extrapolation of the subducted Juan Fernandez ridge beneath the South American plate. The maximum slip distribution from Tilmann et al. (2016) is located between these two relative maximum Tzz, with the main peak located at its center and in coincidence with a relative minima inland. Superimposed aftershock distribution up to April 14, 2016, from USGS catalog (from 5 to 55 km of depth). The diameter of the circle is a function of the magnitude, while *filling* indicates the depth of the hypocenter. Aftershock activity seems to be controlled by the projections of both oceanic features below the margin (as noted by Tilmann et al. (2016) earlier), here depicted by relative maximums in the vertical gravity gradient signal. Rupture propagation also seems to be limited by these relative highs in Tzz probably to the long wavelength characteristic of the GOCE-derived signal

sediments smoothens with depth and that the effect of the Challenger Fz is depicted by a high Tzz signal ( $>+8$  Eötvös) (Fig. 6). These high Tzz values (see Moho depths in Fig. 6) are interpreted as derived from higher densities related to the upwelling of the density structure in the mantle. A relationship is

observed between this Tzz high at approximately 41 km ( $N = 150$ ) and the margin indentation also observed in the inflections of the coastline. At higher degrees ( $N = 250/300$ ), a high Tzz is observed in the upper crust at intermediate depths, which is not related to a topographic high. This is interpreted as

high-density materials intruded by the Challenger Fz. The effect of higher-density materials from the Juan Fernández ridge ( $>+10$  Eötvös) is depicted at slightly shallower depths at 36 km ( $N = 175$ ) than the Challenger Fz. To analyze the combined effect of both bathymetric highs, we calculated Tzz by cutting the harmonic expansion at an intermediate value ( $N = 165$ ) between  $N = 150$  and  $N = 175$ . At the extrapolated path of the subducted Challenger Fz (Fig. 7), a high Tzz (for  $N = 165$ ) is observed. The extrapolation of the Juan Fernandez ridge coincides with an eastward deflection of the positive Tzz contours (mainly the +5 Eötvös). Both Tzz relative maximums roughly correlate with rupture endings. A minimum Tzz is observed inland in coincidence with rupture contours.

The relationship between subducted high oceanic features and earthquake rupture boundaries (along strike or trench perpendicular) has been observed in recent works for the last three megathrust earthquakes along the Chilean margin (Maule 2010, Mw 8.8; Iquique 2014, Mw 8.1; and Illapel 2015, Mw 8.4) based on different data sets. Geersen et al. (2015) reported that several subducted seamounts correlate with the southward and up-dip arrest of the seismic rupture during the 2014 Iquique earthquake. They also found that structural variations in the lower plate influence coupling and seismic rupture offshore northern Chile, whereas the variable structure of the upper plate plays a negligible role. In a recent work, Métois et al. (2016) investigated the link between coupling and seismicity over the Chilean margin ( $38^{\circ}$ – $18^{\circ}$ S) and obtained the first nearly continuous map of interseismic coupling variations on the subduction interface based on GPS networks. They found that for the three (above mentioned) most recent Mw  $>8$  events, coseismic asperities correlate well with highly coupled segments, while low coupling zones (LCZ) behaved as barriers and stopped the ruptures. They found at least six low coupling zones (areas where coupling is low in comparison to neighboring highly coupled segments), five of which correlate with the subduction of ridges or fracture zones of the Nazca plate that enter the trench (Iquique, Baranquilla, La Serena, San Antonio and Arauco LCZs). They also observed that all of them are associated with singularities in the coastline

morphology as peninsulas or bays (often related to crustal fault networks). Particularly, the Illapel earthquake rupture zone spread to the north up to La Serena LCZ (related to Challenger Fz), while to the south it reached the San Antonio LCZ (related to the subduction of the JFR, see Métois et al. (2016) for a detailed analysis).

Contrastingly, Tilmann et al. (2016) proposed that the coseismic rupture was smaller than the gap between these features, arguing against the possibility that the rupture got arrested by either of them. Instead, they highlight that the projections of both oceanic features below the margin seem to mark the limits of significant aftershock activity. Something similar is pointed out by Shinohara et al. (2012) for the Tohoku earthquake.

We plotted (Fig. 7) the aftershock distribution (USGS earthquake catalog <http://earthquake.usgs.gov/earthquakes/search/> up to April 16, 2016) for event magnitudes  $>2.5$ , and hypocenter depth between 5 and 55 km over the vertical gravity gradient map (with  $N = 165$ ). Then we can observe that the aftershock activity decays at a relatively high Tzz signal at the extrapolated path of the subducted Challenger Fz, with no activity north of it (orange dashed line in Fig. 7). A similar situation occurs at the Juan Fernandez ridge inception point, where Tzz contours are deflected eastward. Here, the aftershock activity is nucleated mainly to the north of the +5 Eötvös contour (orange dashed line in Fig. 7). The auscultation depth for  $N = 165$  is about 37.7 km, being the above mentioned Tzz inflexion located at an approximate depth adjacent to the five to six aftershocks between 30 and 40 km of depth (green circles in Fig. 7). Thus, Tzz relative highs and abrupt changes in gravity gradient most probably signal crustal faults along the seismogenic zone.

## 6. Concluding Remarks

Preliminary slip models along the Illapel rupture zone depict a gross latitudinal slip distribution ranging from  $30^{\circ}$ S to  $32.5^{\circ}$ S, which is in agreement with margin segmentation produced by high oceanic features, the Challenger Fz to the north and the Juan Fernandez ridge to the south. The refined model from

Tilman et al. (2016) presents a homogeneous and smaller rupture, centered between the extrapolated paths of both subducted oceanic features. In this region, a nearly sediment-starved trench produces near-to-zero to positive values of  $T_{zz}$ , consequently showing no clear correlation between high slips and low  $T_{zz}$  values, as noted for other events along the Peru–Chilean margin with partially filled trenches (e.g., Valdivia-1960 and Maule-2010: Alvarez et al. 2014; Arequipa-2001, Nazca-1996 and Pisco-2007: Alvarez et al. 2015a). We found that at heavily sedimented segments of the trench (to the South of JFR, for the Maule and Valdivia earthquakes),  $T_{zz}$  relative minima are highly adjusted to slip distribution. At sediment-starved trenches, a gravity diminution (prior to the event) was observed in agreement with the rupture area (for the Iquique–Pisagua earthquakes). For the Illapel event, relative minima were found between two  $T_{zz}$  highs, where maximum slip occurred, noting that slip coincides with a minimum  $T_{zz}$  inland. The  $T_{zz}$  signal shows relative positive values at the inception points of the Juan Fernández ridge and the Challenger Fz at higher depths, which correlate with rupture endings.

The non-removal of the sediment effect from  $T_{zz}$  and the truncation of the degree of the harmonic expansion up to  $N = 225$  allow detecting a  $T_{zz}$  lobe in coincidence with the main rupture. Inland, the higher slip patch between 30°S and 30.5°S is well correlated with a relative minimum  $T_{zz}$  at the forearc region. This is consistent with the results for the Constitución 2010  $M_w = 7.0$  earthquake, being the maximum slips located between two onshore  $T_{zz}$  highs (Alvarez et al. 2014).

Even though a strong relationship between high slips from preliminary models and  $T_{zz}$  lows for the Illapel event have not been found (indeed, there are practically no low  $T_{zz}$  (or  $<0$  Eötvös) values present in this region), as found at other segments of the margin, seismic segmentation related to high oceanic features appears to have a similar influence. The cutting off of the degree/order of the harmonic expansion allowed searching for deeper anomalous mass heterogeneities. The expression developed in Appendix E, allowed determining the auscultation depth or associated depth of a causative mass for a determined degree/order of the spherical harmonic

expansion. In this way, we could relate high  $T_{zz}$  values to the Challenger Fz and to the Juan Fernández ridge, thereby removing shallower anomalies.

Even though a negative  $T_{zz}$  lobe ( $<-1$  Eötvös), located at the extrapolation of the Challenger Fz and depicted at higher degrees of the harmonic expansion ( $N = 250-300$ , i.e., at shallower depths), is most likely related to the presence of underthrust sediments, at lower degrees ( $N = 150/Z_1 \approx 40$  km) a high positive  $T_{zz}$  was found.

This analysis based on the Illapel earthquake leads to highlight the influence of high oceanic features on seismic segmentation, not only at heavily sedimented trenches, but also at sediment-starved segments.

Based on this analysis and on previous results, there seems to be a link between  $T_{zz}$  and slip distribution at relative minima, with relative  $T_{zz}$  highs related to high oceanic features. This favors the hypothesis that structural variations in the lower plate highly influence seismic behavior and seismic segmentation as proposed in previous works (Kelleher and Mc Cann 1976; Lay et al. 1982; Cloos 1992; Cloos and Shreve 1996; Scholz and Small 1997; Bilek 2007; Das and Watts 2009; Watts et al. 2010; Contreras-Reyes and Carrizo 2011; Müller and Landgrebe 2012; Sparkes et al. 2010; Landgrebe and Müller 2015). Particularly, recent observations/studies from the last three  $M > 8$  earthquakes along the Chilean margin show a clear correlation between subducted oceanic features and seismic segmentation by (1) degree of seismic coupling (GPS based Metois et al. 2012, 2013, 2014, 2016), (2) satellite-derived gravity gradients ( $T_{zz}$ -GOCE, Alvarez et al. 2014, 2015a), and (3) seismic data (Geersen et al. 2015).

Similar conclusions based on different data sets highlight the importance of constructing an integrated model combining different methods with different resolutions with the aim to inferring the structure of the seismogenic zone and its seismic cycle.

#### *Acknowledgments*

The authors acknowledge the use of the GMT mapping software of Wessel and Smith (1998) to Dr. Gavin P. Hayes, Research Geophysicist at USGS

National Earthquake Information Center for his useful preliminary slip model, and to Juraj Janak and Blazej Bucha (Department of Theoretical Geodesy, Faculty of Civil Engineering, Slovak University of Technology in Bratislava, Slovakia) for the software (GrafLab) for spherical harmonic synthesis. The authors would like to thank CONICET.

### Appendix 1: The Maule 2010 and Iquique 2014 Earthquakes

The GOCE model GO\_CONS\_GCF\_2\_TIM\_R4 with an effective data volume of approximately 26.5 months from 01/11/2009 to 19/06/2012 and GO\_CONS\_GCF\_2\_TIM\_R5 with an effective data volume of approximately 42 months from 01/11/2009 to 21/10/2013

constitute good tools for studying the Earth gravity field changes after the 27th February 2010 Mw = 8.8 Maule and before the April 1st 2014 Mw = 8.2 Pisagua and April 3rd Mw = 7.7 Iquique earthquakes.

The vertical gravity gradient from GO\_CONS\_GCF\_2\_TIM\_R5 model was compared to the main slip distribution of the Iquique sequence (Schurr et al. 2014) noting that no negative vertical gravity gradient lobes coincide with high slip (Fig. 8a). However, the relative maximum  $T_{zz}$  is observed to the north and south of the main slip patches (as observed for Illapel in this work) and also between both ruptures. When compared, both models calculated up to the same degree/order ( $N = 250$ ) a decrease in the gravity signal in the region where the maximum slip patch occurred, before the occurrence of the event. North and south of both slip patches, an

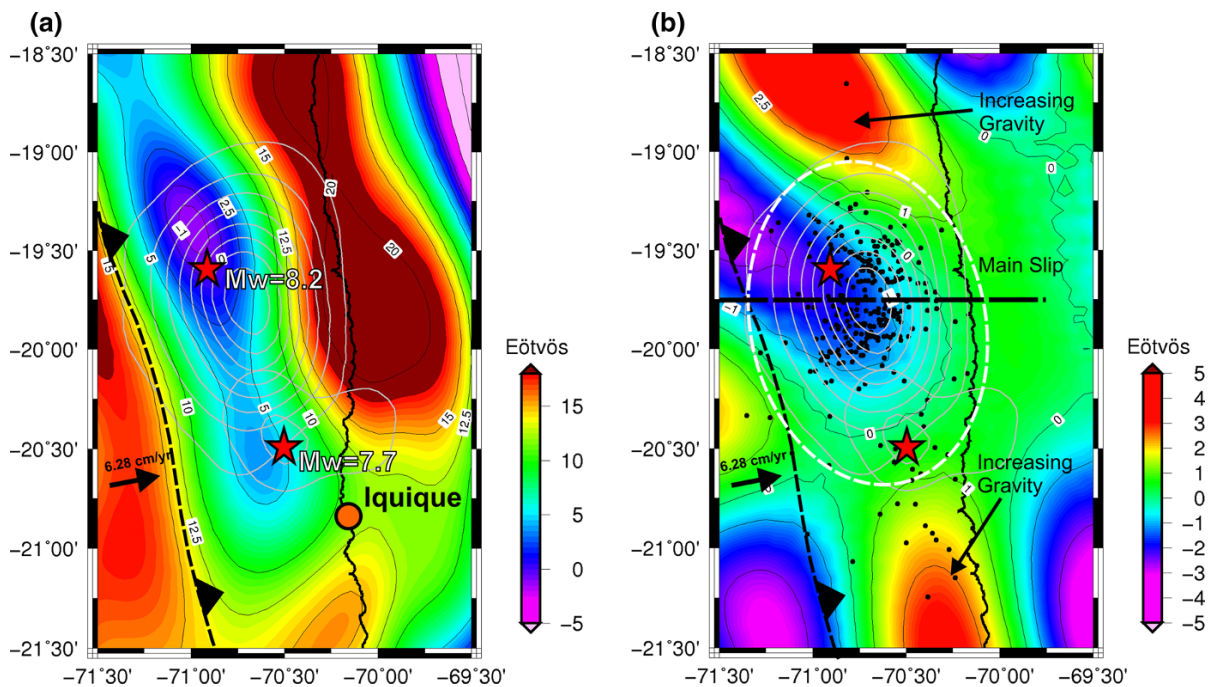


Figure 8

**a** Topography-corrected  $T_{zz}$  obtained from GO\_CONS\_GCF\_2\_TIM\_R5 up to  $N = 250$  compared to slip distribution (solid gray line) from Schurr et al. (2014) for the 2014 Mw = 8.2 Pisagua earthquake and its main aftershock (Mw = 7.7) on Iquique. **b** Residual between R5 and R4 superimposed to the foreshock sequence (ISC-International Seismological Centre) in the region of the 2014 Mw = 8.2 Pisagua and Mw = 7.7 Iquique earthquakes. Black dashed line indicates the profile of Fig. 1a. The residual between both models shows a decrease in the gravity signal (prior to event occurrence) over the maximum slip area with two maxima at its northern and southern terminations (Fig. modified from Alvarez et al. 2015a)

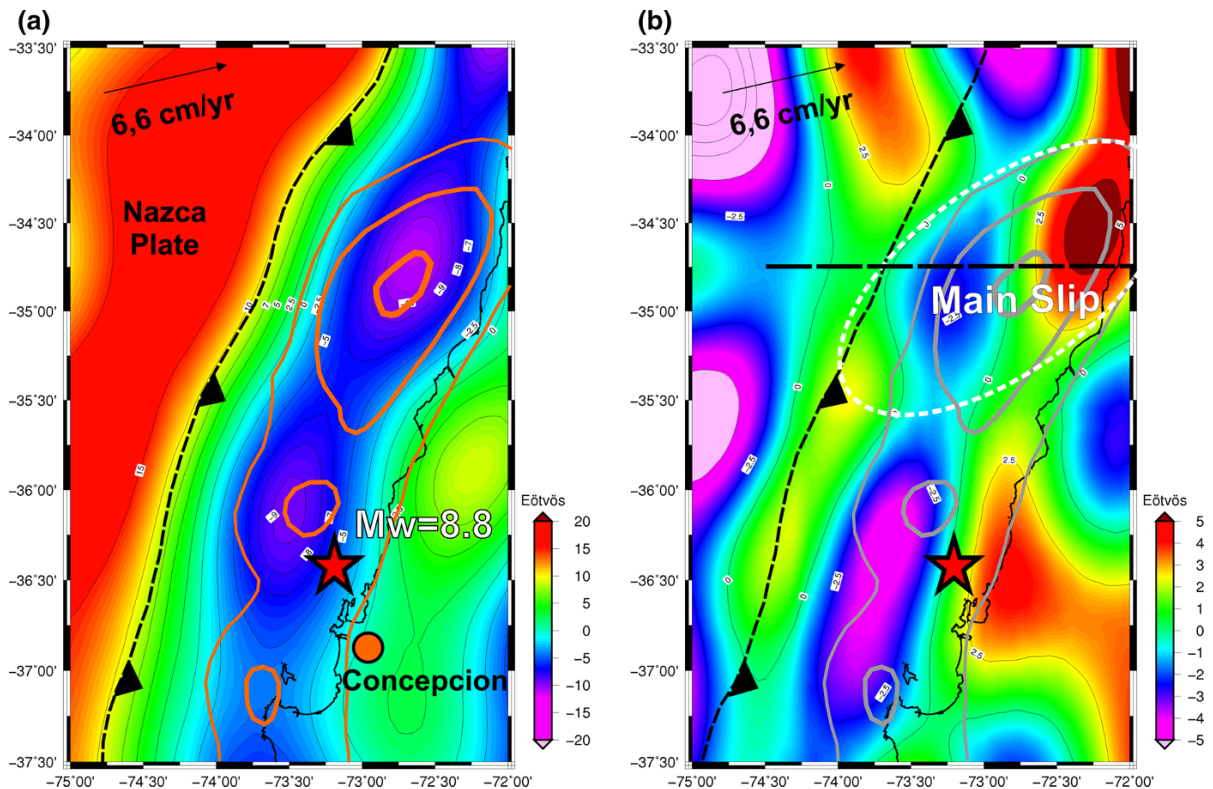


Figure 9

**a** Topography-corrected  $T_{zz}$  obtained from GO\_CONS\_GCF\_2\_TIM\_R4 up to  $N = 250$  compared to slip distribution (orange solid line) from Moreno et al. (2012) for the 2010  $M_w = 8.8$  Maule earthquake. **b** Residual between R5 and R4 in the region of the 2010  $M_w = 8.8$  Maule earthquake. The difference shows that the gravity signal increased in the region of the maximum slip patch for the data time span between 19/6/2012 and 20/10/2013. Black dashed line indicates the profile of Fig. 1b. (Figure modified from Alvarez et al. 2015a)

increase in the gravity gradient signal occurred (see Alvarez et al. 2015a for more details).

For the 2010  $M_w = 8.8$  Maule earthquake, the main slip patches coincide with the minimum  $T_{zz}$  lobes (Fig. 9a) (see Alvarez et al. 2014 for a detailed description). As mentioned above, both GOCE models cover a data span after this event. The residual between both models (Fig. 9b) reveals after the event an increase in  $T_{zz}$  toward the coastline (especially in the area where the main slip occurred), probably indicating uplift of the upper plate due to coseismic and post-seismic lithospheric stretching along the subduction zone. Thus, temporal variations in the gravity field are probably related to either mass redistribution changes or variations in fluid pressure after the 2010  $M_w = 8.8$  Maule and before the 2014  $M_w = 8.2$  Pisagua earthquakes (Alvarez et al. 2015a).

## Appendix 2: Preliminary Slip Models

Rapid estimation of seismic source parameters and preliminary finite-fault slip models for the 16 September 2015 Illapel earthquake were calculated, especially to promptly determine the potential of tsunami genesis and generate the corresponding alerts. The resulting models are quite different (with varying preliminary estimated rupture areas) as these use single data sources in the inversion (e.g., teleseismic wave inversion or geodetic data).

Preliminary finite fault results for the September 16, 2015  $M_w = 8.3$  46 km W of Illapel, Chile earthquake (Version 1) from USGS (Fig. 10a) are based on inversion of the GSN broadband waveforms (26 teleseismic broadband P waveforms, 11 broadband SH waveforms, and 42 long period surface waves from the NEIC waveform server). The

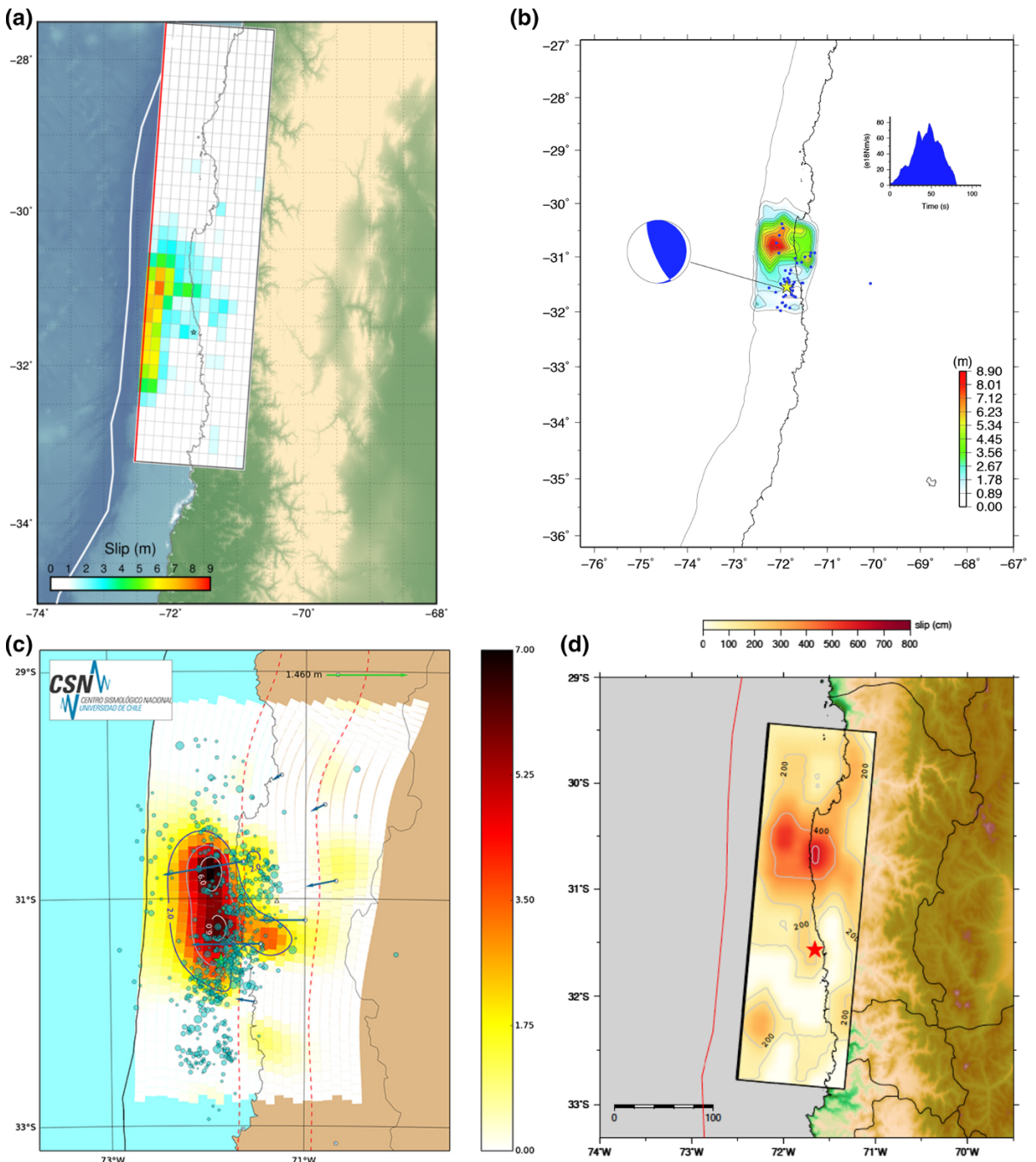


Figure 10

**a** Preliminary surface projection of the slip distribution superimposed on GEBCO bathymetry from USGS. **b** Slip distribution, source time function, epicenter of main shock (*star*), and aftershocks (*blue circles*) from the University of Tsukuba. **c** Estimated coseismic displacement related to the Illapel 2015 earthquake from CSN-Chile. **d** Surface projection of the slip model from the Earth Observatory of Singapore; *red star* indicates the epicenter location and the *rectangle* shows the boundary of the fault plane

waveforms were first converted to displacement by removing the instrument response and are then used to constrain the slip history using a finite fault inverse algorithm (Ji et al. 2002) (see [http://earthquake.usgs.gov/earthquakes/eventpage/us20003k7a-scientific\\_finitefault](http://earthquake.usgs.gov/earthquakes/eventpage/us20003k7a-scientific_finitefault) for more detail). The results show a main slip patch reaching up to 9 m.

Seismic source model of the 2015 off central Chile earthquake (preliminary result) from the University of Tsukuba (<http://www.geol.tsukuba.ac.jp/~yagy/EQ/20150917/index.html>) indicated  $M_w = 8.3$  and fault size of approximately  $150 \text{ km} \times 100 \text{ km}$  (Fig. 10b), with a single main slip patch and reaching approximately 9 m.

Coseismic slip calculated for the Illapel 2015 earthquake and aftershocks processed by the Centro Sismológico Nacional (CSN, <https://www.csn.uchile.cl/estimacion-del-desplazamiento-que-produjo-el-terremoto-de-illapel-2015/>) are shown in Fig. B1c. The maximum slip reaches up to 7 m with two main slip patches. The slip model was obtained by geodetic data inversion (GNSS).

Figure 10d shows the surface projection of the slip model obtained by inversion of 31 teleseismic P waves and 24 SH waves, assuming NEIC epicenter location and W-phase focal mechanism (<http://www.earthobservatory.sg/news/september-16-2015-chile-earthquake>). This model of the kinematic rupture process of the Illapel 2015 earthquake shows a main slip patch with more than 8 m of slip peak and a secondary lobe south of the epicenter.

### *Appendix 3: GOCE Error Assessment*

GOCE gravitational models have global and homogeneous coverage, with well-defined stochastic properties, but are not errorless. We calculated GOCE Tzz errors on a regular grid of  $0.05^\circ$  of cell size, in the local north-oriented reference frame (LNOF) from spherical harmonics coefficients. Calculation was performed in spherical coordinates at satellite (250 km) and calculation (7000 m) heights using WGS84 as the reference system. For error calculation, we used GrafLab (GRAvity Field LABoratory, Bucha and Janák 2013), a novel graphical user interface program for spherical harmonic synthesis

(SHS), which allows computing 38 different functional of the geopotential (including the error propagation) up to ultrahigh degrees and orders of spherical harmonic expansion.

Considering the Tzz signal in the region of study (Fig. 5), between Challenger Fz and Juan Fernandez ridge, which ranges approximately between  $-1$  and  $+7.5$  Eötvös, the error is below 1 % of the signal (Fig. 11b).

### *Appendix 4: Uncertainties Which Should Originate from the Topography and Sediment Corrections*

Removing all possible effects, even small, leads to a “cleaner” signal that allows us to reveal buried structures. Regarding the topographic correction, we used spherical prisms (Heck and Seitz 2007; Asgharzadeh et al. 2007; Wild-Pfeiffer 2008; Uieda et al. 2010; Alvarez et al. 2013; Grombein et al. 2013) instead of a planar approximation (Forsberg 1984; Forsberg and Tscherning 1997; Nagy 1966; Nagy et al. 2000) that greatly reduces calculation errors when calculating big areas since earth curvature is taken into account. Regarding the assumed density, we used a density value of  $2.67 \text{ g/cm}^3$  used in previous works and considered as standard.

The forward calculation of the gravity effect for the sediment package (Fig. 12b) was calculated using a linear approximation with varying densities as depth increases (see Braitenberg et al. 2007). To perform this operation, we used the bathymetry from ETOPO1 (Amante and Eakins 2009) and offshore sediment thickness available from NGDC’s global ocean sediment thickness grid (Whittaker et al. 2013; Divins 2003) which cover homogeneously the offshore region. We considered a mean density of  $2.4 \text{ g/cm}^3$  for sediments which was calculated modeling wide-angle seismic and gravity data (Sallares and Ranero 2005; Ranero et al. 2006). Figures were added showing the magnitude of both corrections (Fig. 12a, b).

The sediment gravity effect has enough impact to be removed to solve buried structures. The sediment correction reaches up to 1.5 Eötvös over the region where sediment thickness is higher (south of JFR) and between 1 and 1.5 Eötvös over the region of the

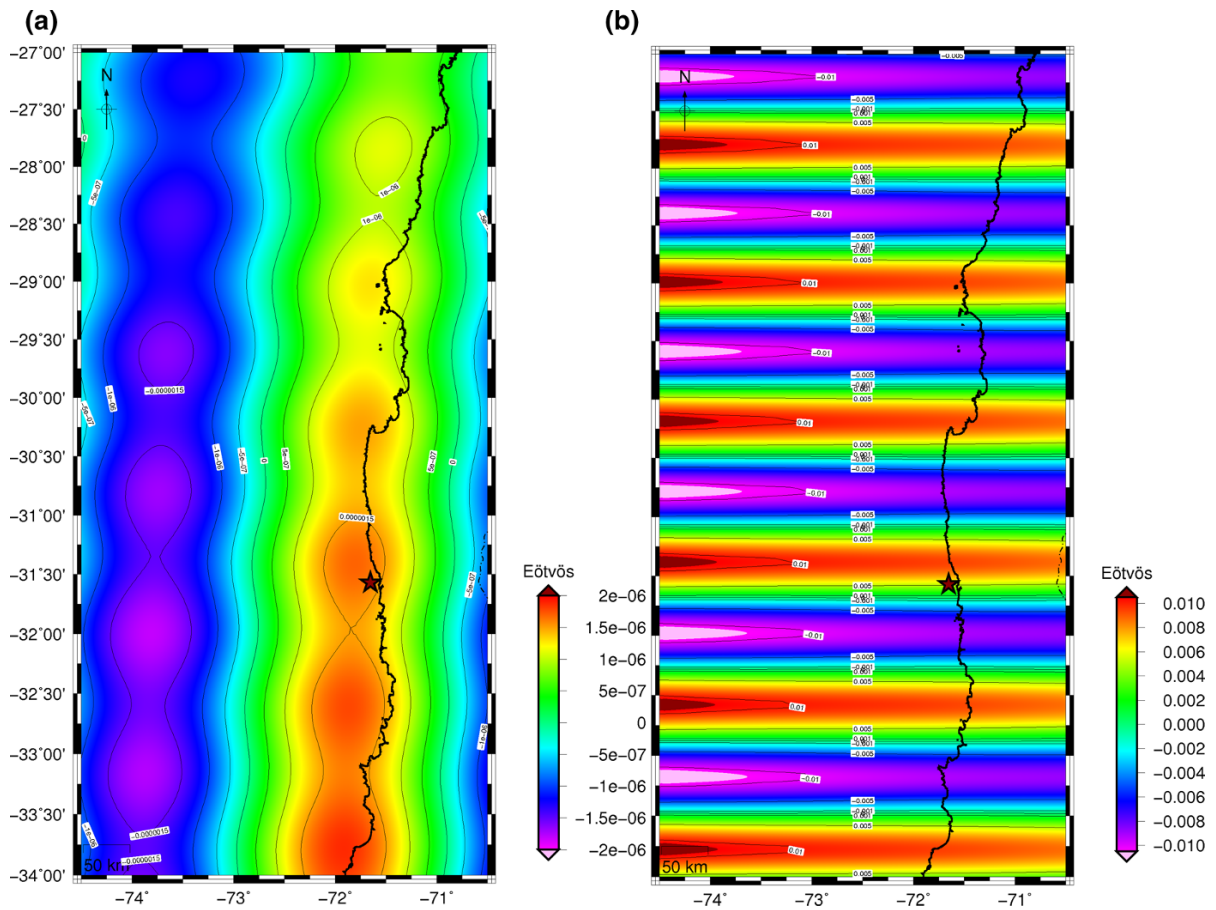


Figure 11

GOCE error for the GO\_CONS\_GCF\_2\_DIR\_R5 (Bruinsma et al. 2013) model calculated at a satellite height of 250 km(a) and at a calculation height of 7000 m (b)

Illapel rupture (Fig. 12b). Figure 13 compares the calculations with and without sediment correction, analyzed with the values of the sediment correction shown in Fig. 12b.

which generates a corresponding geoid wavelength (for a determined degree of the spherical harmonic expansion:  $N$ ).

The maximum depth ( $z$ ) at which a point mass anomaly ( $\delta m$ ) generated the geoid height at the Earth's surface is given by (Bowin 1983):

Appendix 5

$$N = \frac{G\delta m}{z\gamma}, \tag{1}$$

The depth of a mass heterogeneity that generates a determined anomalous potential ( $T$ ) keeps an approximate relationship with the spectral content of the correspondingly derived quantities (e.g., geoid, gravity anomaly, vertical gravity gradient). The analysis of Featherstone (1997) is based on this approximate relationship between the spectral content of the geoid and the depth of a mass density anomaly

where  $G$  is the gravitational constant (Newton) and  $\gamma$  is the normal gravity. Similarly, the gravity anomaly corresponding to the same point mass is:

$$\Delta_g = \frac{G\delta m}{z^2}. \tag{2}$$

Featherstone (1997) combined both equations and obtained the limiting depth at which a point mass can

exist to generate the corresponding observed geoid  $N_{(r,\lambda,\varphi)}$  and gravity anomaly  $\Delta g_{(r,\lambda,\varphi)} = -\frac{\partial T}{\partial r}$  at the Earth's surface,

$$z = \frac{\gamma N}{\Delta g}, \quad (3)$$

and extended to the frequency domain using (Barthelmes 2013):

$$N_{(r,\lambda,\varphi)} = \frac{GM}{r\gamma} \sum_{l=0}^{l_{\max}} \left(\frac{R}{r}\right)^l \sum_{m=0}^l (\bar{C}_{lm} \cos m\lambda + \bar{S}_{lm} \sin m\lambda) \times \bar{P}_{lm} \sin \varphi, \quad (4)$$

Figure 13  
Vertical gravity gradient from GO\_CONS\_GCF\_2\_DIR\_R5 (Bruinsma et al. 2013) compared with surface projection (blue dashed line) of the slip distribution from Tilmann et al. (2016). **a**, **b**  $N = 300$ , **c**, **d**  $N = 250$ , **e**, **f**  $N = 225$ . *Left* without sediment correction. *Right* with sedimentary thickness effect removed

$$\Delta g_{(r,\lambda,\varphi)} = \frac{GM}{r^2} \sum_{l=0}^{l_{\max}} \left(\frac{R}{r}\right)^l (l-1) \times \sum_{m=0}^l (\bar{C}_{lm} \cos m\lambda + \bar{S}_{lm} \sin m\lambda) \times \bar{P}_{lm} \sin \varphi, \quad (5)$$

where  $G$  is the geocentric gravitational constant,  $M$  is the mass of the Earth,  $\gamma$  is the normal gravity on the reference

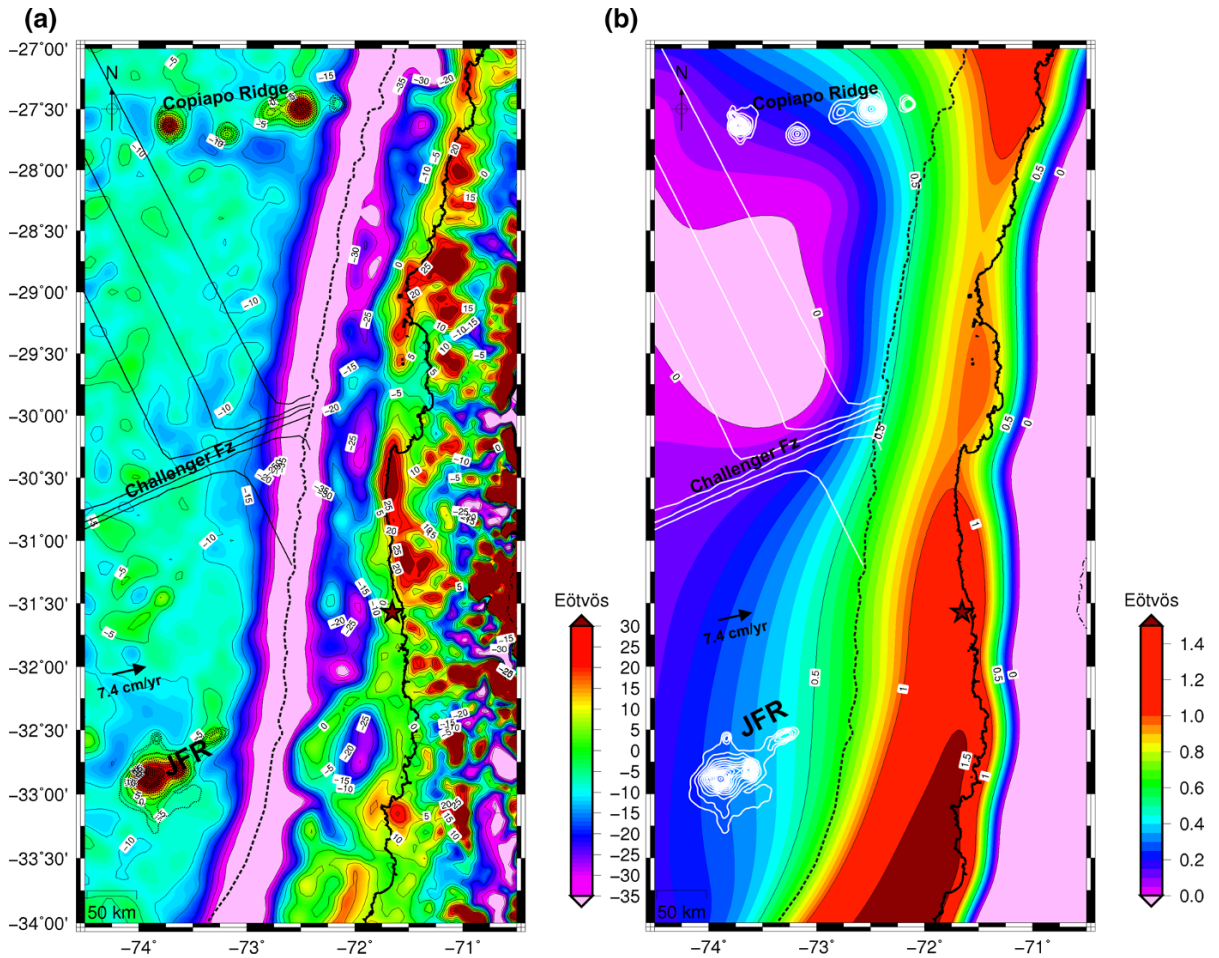
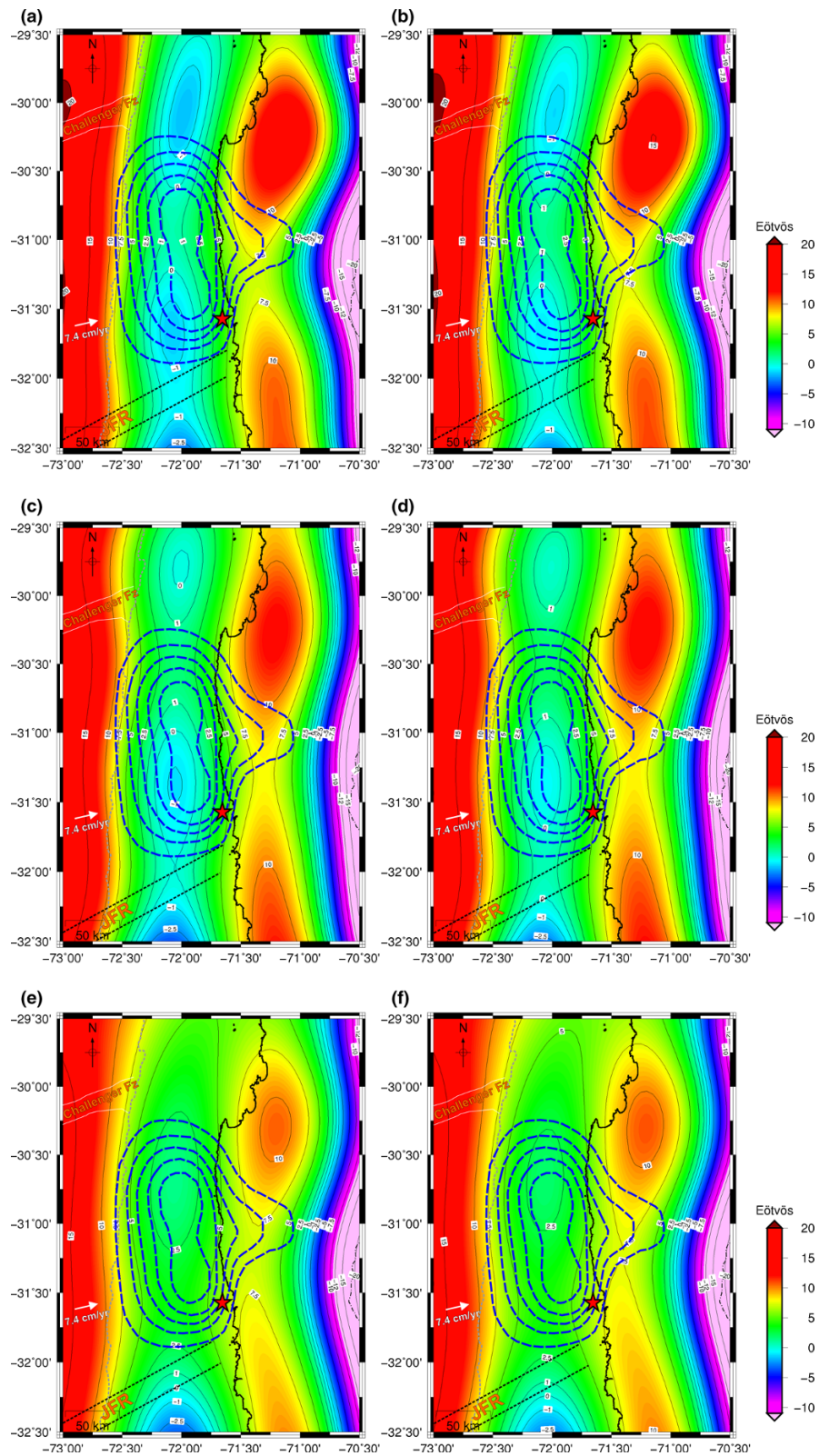


Figure 12

**a** Topographic correction calculated from ETOPO1 (Amante and Eakins 2009) using spherical prisms (Uieda et al. 2010; Alvarez et al. 2013) of constant density ( $2.67 \text{ g/cm}^3$ ). **b** Sediment correction calculated from ETOPO1 and from NGDC's global ocean sediment thickness grid (Whittaker et al. 2013) using a linear approximation with varying densities as depth increases (considering a mean density of  $2.4 \text{ g/cm}^3$ )



ellipsoid,  $(r, \lambda, \varphi)$  are the spherical geocentric coordinates of the computation point (radius, longitude, latitude),  $R$  is the reference radius (mean semi-major axis of the Earth),  $\bar{P}_{lm} \sin \varphi$  are the fully normalized associated Legendre functions of degree  $l$  and order  $m$ , and  $\bar{C}_{lm}$  and  $\bar{S}_{lm}$  are the fully normalized spherical harmonic coefficients (stokes coefficients), which gives an estimate of the maximum depth of a causative mass anomaly as a fraction of the Earth's radius ( $R$ ), corresponding to each spherical harmonic degree. Then:

$$z_l = \frac{R}{(N-1)}. \quad (6)$$

The vertical gravity gradient corresponding to a determined point mass is given by (Wild-Pfeiffer 2008; Grombein et al. 2010):

$$T_{zz} = \frac{2G\delta m}{z^3}. \quad (7)$$

The vertical gravity gradient ( $T_{zz} = \frac{\partial^2 T}{\partial z^2}$ ) can be expressed in a spherical harmonic expansion as the second derivative of the disturbing potential (Barthelmes 2013):

$$T_{(r,\lambda,\varphi)} = \frac{GM}{r} \sum_{l=0}^{l_{\max}} \left(\frac{R}{r}\right)^l \sum_{m=0}^l (\bar{C}_{lm} \cos m\lambda + \bar{S}_{lm} \sin m\lambda) \times \bar{P}_{lm} \sin \varphi, \quad (8)$$

$$T_{zz(r,\lambda,\varphi)} = \frac{2GM}{r^3} \sum_{l=0}^{l_{\max}} \left(\frac{R}{r}\right)^l (l+1)(l+2) \times \sum_{m=0}^l (\bar{C}_{lm} \cos m\lambda + \bar{S}_{lm} \sin m\lambda) \bar{P}_{lm} \sin \varphi. \quad (9)$$

Equations 2 and 7 are now combined to give the limiting depth at which a point mass can exist to generate the corresponding observed gravity anomaly and vertical gravity gradient at the Earth's surface:

$$T_{zz} z^3 = 2\Delta_g z^2. \quad (10)$$

Reorganizing the expression we obtain an equation similar to Eq. 3, but relating  $\Delta_g$  and  $T_{zz}$ :

$$z = \frac{2\Delta_g}{T_{zz}} \quad (11)$$

Extending to the frequency domain by replacing  $\Delta_g$  (Eq. 5) and  $T_{zz}$  (Eq. 9) in Eq. 10:

$$\begin{aligned} z^3 \frac{2GM}{r^3} \sum_{l=0}^{l_{\max}} \left(\frac{R}{r}\right)^l (l+1)(l+2) \\ \times \sum_{m=0}^l (\bar{C}_{lm} \cos m\lambda + \bar{S}_{lm} \sin m\lambda) \bar{P}_{lm} \sin \varphi \\ = 2z^2 \frac{GM}{r^2} \sum_{l=0}^{l_{\max}} \left(\frac{R}{r}\right)^l (l-1) \\ \times \sum_{m=0}^l (\bar{C}_{lm} \cos m\lambda + \bar{S}_{lm} \sin m\lambda) \bar{P}_{lm} \sin \varphi. \end{aligned} \quad (12)$$

Reorganizing:

$$\begin{aligned} \left( \sum_{l=0}^{l_{\max}} \frac{z}{r} \left(\frac{R}{r}\right)^l (l+1)(l+2) - \sum_{l=0}^{l_{\max}} \left(\frac{R}{r}\right)^l (l-1) \right) \\ \times \left( \sum_{m=0}^l (\bar{C}_{lm} \cos m\lambda + \bar{S}_{lm} \sin m\lambda) \bar{P}_{lm} \sin \varphi \right) = 0 \end{aligned} \quad (13)$$

as  $\left( \sum_{m=0}^l (\bar{C}_{lm} \cos m\lambda + \bar{S}_{lm} \sin m\lambda) \bar{P}_{lm} \sin \varphi \right)$ , as spherical harmonic coefficient form a basis in L2, the expression can be overridden only when they do all the coefficients. Therefore, Eq. 15 must hold for all  $l$ :

$$\left( \sum_{l=0}^{l_{\max}} \frac{z}{r} \left(\frac{R}{r}\right)^l (l+1)(l+2) - \sum_{l=0}^{l_{\max}} \left(\frac{R}{r}\right)^l (l-1) \right) = 0, \quad (14)$$

$$\frac{z}{r} \left(\frac{R}{r}\right)^l (l+1)(l+2) - \left(\frac{R}{r}\right)^l (l-1) = 0 \quad \forall l, \quad (15)$$

$$\left( \frac{z}{r} (l+1)(l+2) - (l-1) \right) \left(\frac{R}{r}\right)^l = 0, \quad (16)$$

where  $\left(\frac{R}{r}\right)^l \neq 0$  except for  $r \rightarrow \infty$ ; then at the Earth's surface ( $r = R$ ):

$$Z_l = \frac{R(N-1)}{(N+1)(N+2)}, \quad (17)$$

where  $Z_l$  is the associated depth (for  $l = N$ ),  $R$  is the mean Earth radius and  $N$  the degree/order of the harmonic expansion utilized. As  $T_{zz}$  is calculated above the topographical masses (the Laplace equation is fulfilled in the space outside the masses), we

introduced a correction factor  $H_c$  (calculation height) to the Earth's radius:

$$Z_l = \frac{(R + H_c)(N - 1)}{(N + 1)(N + 2)}. \quad (18)$$

Table 1 computes different associated depths of a causative mass with a determined degree/order of the harmonic expansion for Eqs. 6 and 18 (columns 3 and 4). In Fig. 14a, both expressions are plotted, for

$0 < N < 500$ , depicting that for Tzz the associated depth is shallower than for  $\Delta g$  and geoid for the same degree/order ( $N$ ) of the harmonic expansion. This is as expected, since the vertical gravity gradient (that constitutes a gravity derivative) highlights the superficial density anomalies (Braitenberg et al. 2011; Alvarez et al. 2012). The spectral power of the Tzz signal is pushed to higher frequencies, resulting in a signal more focalized to the source than the Ga

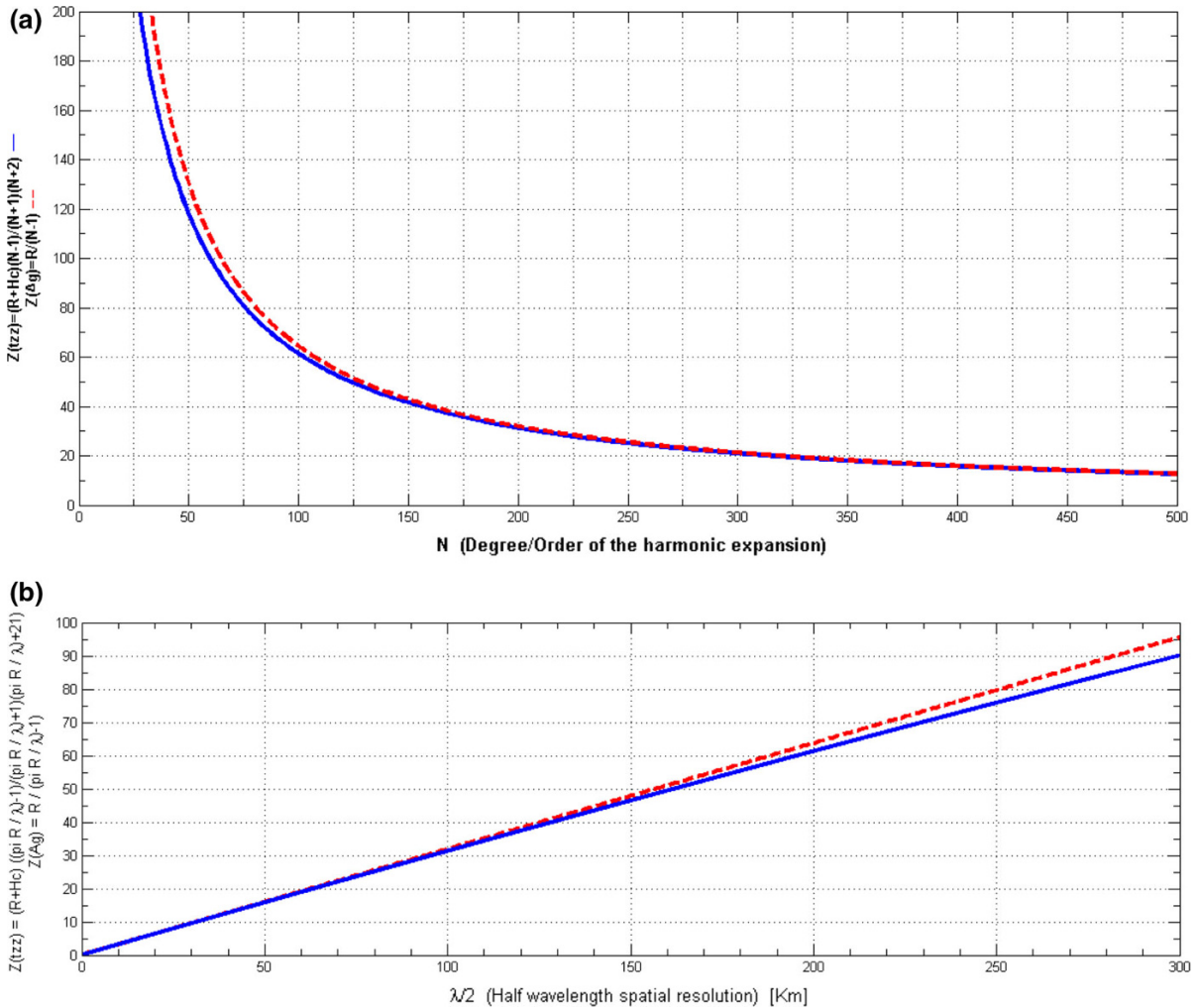


Figure 14

**a** Associated depth ( $Z_l$ ) of a causative mass with a determined degree of the spherical harmonic expansion ( $N$ ) for geoid height and  $\Delta g$  (Featherstone 1997) (red dashed line) and for our derived formulae for Tzz and  $\Delta g$  (blue solid line). Note that with Tzz, the associated depth is shallower than for  $\Delta g$  and geoid for the same degree/order ( $N$ ) of the harmonic expansion. **b** Associated depth ( $Z_l$ ) of a causative mass with a determined half-wavelength spatial resolution (for a determined degree of the spherical harmonic expansion Eq. 19) for geoid height and  $\Delta g$  (Featherstone 1997) (red dashed line) and for our derived formulae for Tzz and  $\Delta g$  (blue solid line). Note that for a determined horizontal spatial resolution, the associated depth is shallower for the Tzz than for  $\Delta g$  and geoid for the same degree/order ( $N$ ) of the harmonic expansion

(Li 2001), with the gravity anomaly being sensitive to regional signals and deeper sources (Álvarez et al. 2012).

The half-wavelength spatial resolution is expressed by Li (2001), Hofmann-Wellenhof and Moritz (2006) and Barthelmes (2013):

$$\lambda/2 = \pi R / N_{\max}, \quad (19)$$

with  $R$  being the mean Earth radius and  $N_{\max}$  the maximum degree/order of the harmonic expansion. So, each degree/order ( $N$ ) corresponds to a determined minimum wavelength (column 2 of Table 1) that can be solved (this wavelength is representative of the respective anomalous mass). By replacing Eq. 19 in Eq. 6 and in Eq. 18, we can express the associated depth ( $Z$ ) of a causative mass with a determined spatial resolution  $\lambda/2$  depending on the degree/order of the utilized spherical harmonic expansion ( $N$ ) (Fig. 14b).

#### REFERENCES

- Abe, K. (1981). Magnitudes of large shallow earthquakes from 1904 to 1980. *Physics Of The Earth And Planetary Interiors*, 27, 72–92.
- Alvarez, O., Gimenez, M. E., Braitenberg, C., & Folguera, A. (2012). GOCE satellite derived gravity and gravity gradient corrected for topographic effect in the South Central Andes region. *Geophysical Journal International*, 190(2), 941–959. doi:10.1111/j.1365-246X.2012.05556.x.
- Alvarez, O., Gimenez, M. E., & Braitenberg, C. (2013). Nueva metodología para el cálculo del efecto topográfico para la corrección de datos satelitales. *Revista de la Asociación Geológica Argentina*, 70(4), 422–429.
- Alvarez, O., Nacif, S., Gimenez, M., Folguera, A., & Braitenberg, A. (2014). Goce derived vertical gravity gradient delineates great earthquake rupture zones along the Chilean margin. *Tectonophysics*, 622, 198–215. doi:10.1016/j.tecto.2014.03.011.
- Alvarez, O., Nacif, S., Spagnotto, S., Folguera, A., Gimenez, M., Chlieh, M., Braitenberg, C. (2015a). Gradients from GOCE reveal gravity changes before Pisagua Mw =8.2 and Iquique Mw =7.7 large megathrust earthquakes. *Journal of South American Earth Sciences*, 64P2, 15–29. <http://dx.doi.org/10.1016/j.jsames.2015.09.014>
- Alvarez, O., Gimenez, M. E., Martínez, M. P., LinceKlinger, F., Braitenberg, C., (2015b). New insights into the Andean crustal structure between 32° and 34°S from GOCE satellite gravity data and EGM2008 model. In: Sepúlveda, S.A., Giambiagi, L.B., Moreiras, S.M., Pinto, L., Tunik, M., Hoke, G.D., Fariás, M., (Eds.), *Geodynamic Processes in the Andes of Central Chile and Argentina* 399, pp. 183–202. London: Geological Society, Special Publications. <http://dx.doi.org/10.1144/SP399.3>
- Alvarez, O., Gimenez, M., Folguera, A., Spagnotto, S., Bustos, E., Baez, W., et al. (2015c). New evidence about the subduction of the Copiapó ridge beneath South America, and its connection with the Chilean-Pampean flat slab, tracked by satellite GOCE and EGM2008 models. *Journal of Geodynamics*, 91C, 65–88. doi:10.1016/j.jog.2015.08.002.
- Amante, C., Eakins, B.W., (2009). ETOPO1, 1 Arc-Minute Global Relief Model: Procedures, Data Sources and Analysis. NOAA Technical Memorandum NESDIS NGDC-24, pp. 19
- ANCORP Working Group. (2003). Seismic imaging of a convergent continental margin and plateau in the central Andes (Andean Continental Research Project 1996 (ANCORP'96)). *Journal Geophysical Research*, 108(B7), 2328. doi:10.1029/2002JB001771.
- Asgharzadeh, M. F., Von Frese, R. R. B., Kim, H. R., Leftwich, T. E., & Kim, J. W. (2007). Spherical prism gravity effects by Gauss-Legendre quadrature integration. *Geophysical Journal International*, 169, 1–11. doi:10.1111/j.1365-246X.2007.03214.x.
- Bangs, N. L., & Cande, S. C. (1997). Episodic development of a convergent margin inferred from structures and processes along the southern Chile margin. *Tectonics*, 16(3), 489–505.
- Barrientos, S. E. (1988). Slip distribution of the 1985 Central Chile earthquake. *Tectonophysics*, 145(3–4), 225–241. doi:10.1016/0040-1951(88)90197-7.
- Barrientos, S. E. (1995). Dual seismogenic behaviour: the 1985 central Chile earthquake. *Geophysical Research Letters*, 22, 3541–3544. doi:10.1029/95GL03316.
- Barthelmes, F., 2013. Definition of functionals of the geopotential and their calculation from spherical harmonic models. Theory and formulas used by the calculation service of the International Centre for Global Earth Models (ICGEM). Scientific Technical Report, STR09/02, Revised edition, January 2013. GFZ German Research Centre for Geosciences, Postdam, Germany. <http://icgem.gfz-postdam.de/ICGEM>
- Beck, S., Barrientos, S., Kausel, E., & Reyes, M. (1998). Source characteristics of historic earthquakes along the central Chile subduction zone. *Journal of South American Earth Sciences*, 11, 115–292.
- Bedford, J., Moreno, M., Schurr, B., Bartsch, M., & Oncken, O. (2015). Investigating the final seismic swarm before the Iquique-Pisagua 2014 Mw 8.1 by comparison of continuous GPS and seismic foreshock data. *Geophysical Research Letters*, 42, 3820–3828. doi:10.1002/2015GL063953.
- Bilek, S.L., (2007). Influence of subducting topography on earthquake rupture. In: Dixon, T. and C. Moore. (Eds.) *The Seismogenic Zone of Subduction Thrust Faults* (pp. 123–146). New York: Columbia University.
- Bomfim, E. P., Braitenberg, C., & Molina, E. C. (2013). Mutual evaluation of global gravity models (EGM2008 and GOCE) and terrestrial data in Amazon Basin, Brazil. *Geophysical Journal International*, 195(2), 870–882. doi:10.1093/gji/ggt283.
- Bouman, J., Ebbing, J., & Fuchs, M. (2013). Reference frame transformation of satellite gravity gradients and topographic mass reduction. *Journal of Geophysical Research: Solid Earth*, 118(2), 759–774. doi:10.1029/2012JB009747.
- Bowin, C. O. (1983). Depth of principal mass anomalies contributing to the Earth's geoid undulations and gravity anomalies. *Marine Geodesy*, 7, 61–100.
- Braitenberg, C., Wienecke, S., Ebbing, J., Bom, W., & Redfield, T. (2007). Joint gravity and isostatic analysis for basement studies—a novel tool. In: EGM. *International Workshop, Innovation*

- in *EM, Grav and Mag Methods: a new perspective for exploration*. Capri: Villa Orlandi. **(Extended Abstracts)**.
- Braitenberg, C., Mariani, P., Ebbing, J., Sprlak, M., (2011). The enigmatic Chad lineament revisited with global gravity and gravity-gradient fields. In: D.J.J. Van Hinsbergen, S.J.H. Buiter, T.H. Torsvik, C. Gaina and S.J. Webb. (Eds.), *The formation and evolution of Africa: a synopsis of 3.8 Ga of Earth History*, Vol. 357, pp. 329–341. London: Geological Society, Special Publication. doi:10.1144/SP357.18
- Bruinsma, S.L., Marty, J.C., Balmino, G., Biancale, R., Förste, C., Abrikosov, O., Neumayer, H. (2010). GOCE gravity field recovery by means of the direct numerical method. In: Lacoste-Franis H (ed) *Proceedings of the ESA living planet symposium*, (27) SP-686. Bergen, Norway: ESA Publication.
- Bruinsma, S. L., Förste, C., Abrikosov, O., Marty, J. C., Rio, M. H., Mulet, S., et al. (2013). The new ESA satellite-only gravity field model via the direct approach. *Geophysical Research Letters*, 40, 3607–3612.
- Bucha, B., & Janák, J. (2013). A MATLAB-based graphical user interface program for computing functionals of the geopotential up to ultra-high degrees and orders. *Computers & Geosciences*, 56, 186–196. doi:10.1016/j.cageo.2013.03.012.
- Bürgmann, R. (2014). Warning signs of the Iquique earthquake. *Nature*, 512, 258–259.
- Cahill, T., & Isacks, B. (1992). Seismicity and shape of the subducted Nazca plate. *Journal Geophysical Research*, 97(B12), 17503–17529.
- Cesca, S., Grigoli, F., Heimann, S., Dahm, T., Kriegerowski, M., Sobiesiak, M., et al. (2016). The Mw 8.1 2014 Iquique, Chile, seismic sequence: a tale of foreshocks and aftershocks. *Geophysical Journal International*, 204, 1766–1780. doi:10.1093/gji/ggv544.
- Christensen, D. H., & Ruff, L. J. (1986). Rupture process of the March 3, 1985 Chilean earthquake. *Geophysical Research Letters*, 13, 721–724.
- Cloos, M. (1992). Thrust-type subduction zone earthquakes and seamount asperities: a physical model for seismic rupture. *Geology*, 20(7), 601–604.
- Cloos, M., & Shreve, R. L. (1996). Shear-zone thickness and the seismicity of Chilean- and Marianas-type subduction zones. *Geology*, 24(2), 107–110.
- Comte, D., Eisenberg, A., Lorca, E., Pardo, M., Ponce, L., Saragoni, R., et al. (1986). The 1985 Central Chile earthquake: a repeat of previous great earthquakes in the region? *Science*, 233, 449–453. doi:10.1126/science.233.4762.449.
- Contreras-Reyes, E., & Carrizo, D. (2011). Control of high oceanic features and subduction channel on earthquake ruptures along the Chile-Peru subduction zone. *Physics of the Earth and Planetary Interiors*, 186, 49–58.
- Contreras-Reyes, E., Flueh, E., & Grevemeyer, L. (2010). Tectonic control on sediment accretion and subduction off south-central Chile: Implications for coseismic rupture processes of the 1960 and 2010 megathrust earthquakes. *Tectonics*, 29, TC6018.
- Das, S., & Watts, A. B. (2009). Effect of subducting seafloor topography on the rupture characteristics of great subduction zone earthquakes. In S. Lallemand & F. Funiciello (Eds.), *Subduction Zone Geodynamics* (pp. 103–118). Berlin-Heidelberg: Springer-Verlag.
- DeMets, C., Gordon, R. G., & Argus, D. F. (2010). Geologically current plate motions. *Geophysical Journal International*, 181, 1–80.
- Divins, D. L. (2003). *Total Sediment Thickness of the World's Oceans and Marginal Seas*. Boulder CO: NOAA National Geophysical Data Center.
- Featherstone, W. (1997). On the use of the geoid in geophysics: a case study over the northwest shelf of Australia. *Exploration Geophysics*, 28(1/2), 52–57.
- Flueh, E. R., Vidal, N., Ranero, C. R., Hokja, A., von Huene, R., Bialas, J., et al. (1998). Seismic investigation of the continental margin off- and onshore Valparaiso, Chile. *Tectonophysics*, 288, 251–263.
- Forsberg, R., (1984). A study of terrain reductions, density anomalies and geophysical inversion methods in gravity field modeling, Scientific Report N. 5, AFGL-TR-84-0174, Department of Geodetic Science and Surveying, pp. 133. Columbus: Ohio State University.
- Forsberg, R. & Tscherning, C.C., (1997). Topographic effects in gravity modeling for BVP, In: F. Sanso & R. Rummel (Eds.), *Geodetic Boundary Value Problems in View of the One Centimeter Geoid*, Lecture Notes in Earth Science, Vol. 65, pp. 241–272. Berlin: Springer.
- Fuchs, M. J., Bouman, J., Broerse, T., Visser, P., & Vermeersen, B. (2013). Observing coseismic gravity change from the Japan Tohoku-Oki 2011 earthquake with GOCE gravity gradiometry. *Journal of Geophysical Research: Solid Earth*, 118, 1–10. doi:10.1002/jgrb.50381.
- Geersen, J., Ranero, C., Barkhausen, U., & Reichert, C. (2015). Subducting seamounts control interplate coupling and seismic rupture in the 2014 Iquique earthquake area. *Nature Communications*, 6, 8267. doi:10.1038/ncomms9267.
- Grombein, T., Heck, B., & Seitz, K. (2010). Untersuchungen zur effizienten Berechnung topographischer Effekte auf den Gradiententensor am Fallbeispiel der Satelliten gradiometrie mission GOCE. Karlsruhe Institute of Technology, KIT Scientific Reports 7547, pp. 1–94, ISBN 978-3-86644-510-9.
- Grombein, T., Seitz, K., & Heck, B. (2013). Optimized formulas for the gravitational field of a tesseroid. *Journal of Geodesy*, 87(7), 645–660.
- Heck, B., & Seitz, K. (2007). A comparison of the tesseroid, prism and point mass approaches for mass reductions in gravity field modeling. *Journal of Geodesy*, 81(2), 121–136. doi:10.1007/s00190-006-0094-0.
- Heuret, A., Conrad, C. P., Funiciello, F., Lallemand, S., & Sandri, L. (2012). Relation between subduction megathrust earthquakes, trench sediment thickness and upper plate strain. *Geophysical Research Letters*, 39, L05304. doi:10.1029/2011GL050712.
- Hofmann-Wellenhof, B., Moritz, H., (2006). *Physical Geodesy*, 2nd edn, pp. 286. Berlin: Springer.
- Hyndman, G. C., Dragert, H., Wrang, K., Clague, J. J., Adams, J., & Bobrowsky, P. T. (1996). Giant Earthquakes beneath Canada's West Coast. *Geosciences Canada*, 23(2), 63–72.
- Janak, J., & Sprlak, M. (2006). New software for gravity field modelling using spherical harmonic. *Geodetic and Cartographic Horizon*, 52, 1–8. **(in Slovak)**.
- Ji, C., Wald, D. J., & Helmberger, D. V. (2002). Source description of the 1999 Hector Mine, California earthquake; Part I: wavelet domain inversion theory and resolution analysis. *Bulletin of the Seismological Society of America*, 92(4), 1192–1207.
- Kelleher, J. A. (1972). Rupture zones of large South American earthquakes and some predictions. *Journal Geophysical Research*, 77, 2087–2103.

- Kelleher, J., & Mc Cann, W. (1976). Buoyant zones, great earthquakes, and unstable boundaries of subduction. *Journal Geophysical Research*, *81*, 4885–4896.
- Kendrick, E., Bevis, M., Smalley, R., & Brooks, B. (2001). An integrated crustal velocity field for the Central Andes. *Geochemistry, Geophysics, Geosystems*, *2*, 1066. doi:10.1029/2001GC000191.
- Kendrick, E., Bevis, M., Smalley, R., Brooks, B., Barriga, R., & Lauri, E. (2003). The Nazca-south America Euler vector and its rate of change. *Journal of South American Earth Sciences*, *16*, 125–131.
- Kodaira, S., Takahashi, N., Nakanishi, A., Miura, S., & Kaneda, Y. (2000). Subducted seamount imaged in the rupture zone of the 1946 Nankaido earthquake. *Science*, *289*, 104–106.
- Kopp, H. (2013). Invited review paper: the control of subduction zone structural complexity and geometry on margin segmentation and seismicity. *Tectonophysics*, *589*, 1–16. doi:10.1016/j.tecto.2012.12.037.
- Lamb, S., & Davis, P. (2003). Cenozoic climate change as a possible cause for the rise of the Andes. *Nature*, *425*, 792–797.
- Landgrebe, T. C. W., & Müller, R. D. (2015). Uncovering the relationship between subducting bathymetric ridges and volcanic chains with significant earthquakes using geophysical data mining. *Australian Journal of Earth Sciences*, *62*, 171180. doi:10.1080/08120099.2015.1003145.
- Laursen, J., Scholl, D. W., & von Huene, R. (2002). Neotectonic deformation of the central Chile margin: deepwater forearc basin formation in response to hot spot ridge and seamount subduction. *Tectonics*, *21*(5), 1038. doi:10.1029/2001TC901023.
- Lay, T., Kanamori, H., & Ruff, L. (1982). The asperity model and the nature of large subduction zone earthquakes. *Earthquake Prediction Research*, *1*, 3–71.
- Lay, T., Yue, H., Brodsky, E. E., & An, C. (2014). The 1 April 2014 Iquique, Chile, Mw 8.1 earthquake rupture sequence. *Geophysical Research Letters*, *41*, 3818–3825. doi:10.1002/2014GL060238.
- Li, X. (2001). Vertical resolution: gravity versus vertical gravity gradient. *The Leading Edge*, *20*, 901–904.
- Llenos, A. L., & Mc Guire, J. J. (2007). Influence of fore-arc structure on the extent of great subduction zone earthquakes. *Journal Geophysical Research*, *112*, B09301.
- Lohrmann, J., Kukowski, N., Krawczyk, C. M., Oncken, O., Sick, C., Sobiesiak, M., et al. (2006). Subduction channel evolution in brittle fore-arc wedges—a combined study with scaled sandbox experiments, seismological and reflection seismic data and geological field evidence. In O. Oncken, G. Chong, G. Franz, P. Giese, H.-J. Götze, V. A. Ramos, M. R. Strecker, & P. Wigger (Eds.), *The andes—active subduction orogeny. Frontiers in earth science series* (pp. 237–262). Berlin, Heidelberg, New York: Springer.
- Maksymowicz, A., Tréhuc, A., Contreras-Reyes, E., & Ruiz, S. (2015). Density-depth model of the continental wedge at the maximum slip segment of the Maule Mw8.8 megathrust earthquake. *Earth and Planetary Science Letters*, *409*, 265–277. doi:10.1016/j.epsl.2014.11.005.
- Mendoza, C., Hartzell, S., & Monfret, T. (1994). Wide band analysis of the 3 March 1985 central Chile earthquake: overall source process and rupture history. *Bulletin of the Seismological Society of America*, *84*, 269–283.
- Métis, M., Socquet, A., Vigny, C., Carrizo, D., Peyrat, S., Delorme, A., et al. (2013). Revisiting the North Chile seismic gap segmentation using GPS-derived interseismic coupling. *Geophysical Journal International*, *194*, 1283–1294. doi:10.1093/gji/ggt183.
- Métis, M., Socquet, A., & Vigny, C. (2012). Interseismic coupling, segmentation and mechanical behavior of the central Chile subduction zone. *Journal of Geophysical Research*.doi:10.1029/2011JB008736.
- Métis, M., Vigny, C., Socquet, A., Delorme, A., Morvan, S., Ortega, I., et al. (2014). GPS-derived interseismic coupling on the subduction and seismic hazards in the Atacama region, Chile. *Geophysical Journal International*, *196*(2), 644–655. doi:10.1093/gji/ggt418.
- Métis, M., Vigny, C., & Socquet, A. (2016). Interseismic coupling, megathrust earthquakes and seismic swarms along the Chilean subduction zone (38°–18°S). *Pure and Applied Geophysics*. doi:10.1007/s00024-016-1280-5. (in press).
- Montessus de Ballore, F. 1912. Historia sísmica de los Andes meridionales al sur del paralelo XVI. Anales de la Universidad de Chile, Vol. 4, p. 2. Santiago de Chile: Editorial Cervantes.
- Moreno, M. S., Melnick, D., Rosenau, M., Baez, J., Klotz, J., Oncken, O., Tassara, A., Chen, J., Bataille, K., Bevis, M., Socquet, A., Bolte, J., Vigny, C., Brooks, B., Ryder, I., Grund, V., Smalley, B., Carrizo, D., Bartsch, M., & Hase, H. (2012). Toward understanding tectonic control on the Mw 8.8 2010 Maule Chile earthquake. *Earth and Planetary Science Letters*, *321*–322, 152–165. doi:10.1016/j.epsl.2012.01.006.
- Moreno, M., Bartsch, M., Zhang, Y., Oncken, O., Tilmann, F., Dahm, T., et al. (2014). Gradual unlocking of plate boundary controlled initiation of the 2014 Iquique earthquake. *Nature*, *512*, 299–302. doi:10.1038/nature13681.
- Mulcahy, P., Chen, C., Kay, S., Brown, L., Isacks, B., Sandvol, E., et al. (2015). Central Andean Mantle and crustal seismicity under the Southern Puna plateau and Northern Margin of the Chilean Flatslab. *Tectonics*. doi:10.1002/2013TC003393. (in press).
- Müller, R. D., & Landgrebe, T. C. W. (2012). The link between great earthquakes and the subduction of oceanic fracture zones. *Solid Earth*, *3*, 447–465. doi:10.5194/se-3-447-2012.
- Müller, R. D., Sdrolias, M., Gaina, C., & Roest, W. R. (2008). Age, spreading rates and spreading symmetry of the world's ocean crust. *Geochemistry, Geophysics, Geosystems*, *9*, Q04006. doi:10.1029/2007GC001743.
- Nagy, D. (1966). The gravitational attraction of a right rectangular prism. *Geophysics*, *31*(2), 362–371.
- Nagy, D., Papp, G., & Benedek, J. (2000). The gravitational potential and its derivatives for the prism. *Journal of Geodynamics*, *74*(7–8), 552–560. doi:10.1007/s001900000116.
- Nishenko, S. P. (1985). Seismic Potential for large and great interplate earthquakes along the Chilean and southern Peruvian margins of South America. A quantitative reappraisal. *Journal of Geophysical Research*, *90*, 3589–3615.
- Pail, R., Bruinsma, S., Migliaccio, F., Förste, C., Goiginger, H., Schuh, W. D., et al. (2011). First GOCE gravity field models derived by three different approaches. *Journal of Geodesy*, *85*, 819–843.
- Ranero, C., von Huene, R., Weinrebe, W., & Reichert, C. (2006). Tectonic Processes along the Chile Convergent Margin. In O. Oncken, G. Chong, G. Franz, P. Giese, H. J. Götze, V. A. Ramos, M. R. Strecker, & P. Wigger (Eds.), *The andes—active subduction orogeny. Frontiers in earth science series* (pp. 91–121). Berlin, Heidelberg, New York: Springer.

- Ruff, L. J. (1989). Do trench sediments affect great earthquake occurrence in subduction zones? *Pure and Applied Geophysics*, *129*, 263–282.
- Ruiz, S., Grandin, R., Dionicio, V., Satriano, C., Fuenzalida, A., Vignyc, C., et al. (2013). The Constitución earthquake of 25 March 2012: a large aftershock of the Maule earthquake near the bottom of the seismogenic zone. *Earth and Planetary Sciences Letters*, *377–378*, 347–357.
- Ruiz, S., Métois, M., Fuenzalida, A., Ruiz, J., Leyton, F., Grandin, R., et al. (2014). Intense foreshocks and a slow slip event preceded the 2014 Iquique mw 8.1 earthquake. *Science*, *345*(6201), 1165–1169. doi:10.1126/science.1256074.
- Sallares, V., & Ranero, C. R. (2005). Structure of the North Chile erosional convergent margin off Antofagasta (23°30'S). *Journal Geophysical Research*. doi:10.1029/2004JB003418.
- Sandwell, D. T., & Smith, W. H. F. (1997). Marine gravity anomaly from Geosat and ERS-1 satellite altimetry. *Journal of Geophysical Research*, *102*, 10039–10050.
- Schertwath, M., Contreras-Reyes, E., Flueh, E., Grevemeyer, J., Krabbenhoft, A., Papenberg, C., et al. (2009). Deep lithospheric structures along the southern central Chile margin from wide-angle P-wave modelling. *Geophysical Journal International*, *179*(1), 579–600.
- Scholl, D., Huene, R., Kirby, S., (2010). The Aleutian Alaska subduction zone is prone to rupture in great and giant megathrust earthquakes—how scientific information can mitigate consequences. Newsletter of the Alaska Geological Society BP Energy Center.
- Scholz, C. H., & Small, C. (1997). The effect of seamount subduction on seismic coupling. *Geology*, *25*(6), 487–490.
- Schurr, B., Asch, G., Hainzl, S., Bedford, J., Hoehner, A., Palo, M., et al. (2014). Gradual unlocking of plate boundary controlled initiation of the 2014 Iquique earthquake. *Nature*, *512*, 299–302. doi:10.1038/nature13681.
- Schweller, W.J., Kulm, L.D., Prince, R.A. 1981. Tectonics structure, and sedimentary framework of the Perú-Chile Trench. In: Kulm LD, et al. (Eds). Nazca Plate: Crustal formation and Andean convergence. *Memories of Geological Society America* *154*:323–349
- Shinohara, M., Machida, Y., Yamada, T., Nakahigashi, K., Shinbo, T., Mochizuki, K., et al. (2012). Precise aftershock distribution of the 2011 off the Pacific coast of Tohoku Earthquake revealed by an ocean-bottom seismometer network. *Earth Planets Space*, *64*(12), 1137–1148. doi:10.5047/eps.2012.09.003.
- Sobiesak, M., Meyer, U., Schmidt, S., Götze, H. J., & Krawczyk, C. (2007). Asperity generating upper crustal sources revealed by *b*-value and isostatic residual anomaly grids in the area of Antofagasta. *Journal Geophysical Research*, *112*, B12308. doi:10.1029/2006JB004796.
- Song, T. R., & Simons, M. (2003). Large trench-parallel gravity variations predict seismogenic behavior in subduction zones. *Science*, *301*, 630–633.
- Sparkes, R., Tilmann, F., Hovius, N., & Hillier, J. (2010). Subducted seafloor relief stops rupture in South American great earthquakes: implications for rupture behaviour in the 2010 Maule, Chile earthquake. *Earth and Planetary Science Letters*, *298*, 89–94. doi:10.1016/j.epsl.2010.07.029.
- Tassara, A. (2010). Control of forearc density structure on megathrust shear strength along the Chilean subduction zone. *Tectonophysics*, *495*, 34–47. doi:10.1016/j.tecto.2010.06.004.
- Tilmann, F., Zhang, Y., Moreno, M., Saul, J., Eckelmann, F., Palo, M., et al. (2016). The 2015 Illapel earthquake, central Chile: a type case for a characteristic earthquake? *Geophysical Research Letters*, *43*, 574–583. doi:10.1002/2015GL066963.
- Uieda, L., Ussami, N., Braitenberg, C.F., (2010). Computation of the gravity gradient tensor due to topographic masses using tesserooids. *Eos Trans. AGU*, *91* (26). Meeting America Supply, Abstract G22A-04. <http://code.google.com/p/tesserooids/>
- Völker, D., Wiedicke, M., Ladage, S., Gaedicke, C., Reichert, C., Rauch, K., Kramer, W., Heubeck, C., (2006). Latitudinal Variation in Sedimentary Processes in the Peru-Chile Trench off Central Chile. In Oncken et al. (Eds.), *The Andes- Active Subduction Orogeny*, *Frontiers in Earth Science Series, Part II*, pp. 193–216. Berlin Heidelberg New York: Springer-Verlag. doi:10.1007/978-3-540-48684-8\_9.
- Von Huene, R., Corvalán, J., Flueh, E.R., Hinz, K., Korstgard, J., Ranero, C.R., Weinrebe, W., CONDOR scientists, 1997. Tectonic control of the subducting Juan Fernández Ridge on the Andean margin near Valparaiso, Chile. *Tectonics* *16* (3), 474–488.
- Wang, K., & Bilek, S. (2011). Do subducting seamounts generate or stop large earthquakes? *Geology*, *39*, 819–822. doi:10.1130/G31856.1.
- Watts, A. B., Koppers, A. A. P., & Robinson, D. P. (2010). Seamount subduction and earthquakes. *Oceanography*, *23*(1), 166–173.
- Wells, R. E., Blakely, R. J., Sugiyama, Y., Scholl, D. W., & Dinterman, P. A. (2003). Basin centered asperities in great subduction zone earthquakes: a link between slip, subsidence and subduction erosion? *Journal Geophysical Research*, *108*(B10), 2507–2536. doi:10.1029/2002JB002072.
- Wessel, P., & Smith, W. H. F. (1998). New, Improved Version of the Generic Mapping Tools Released. *EOS Transactions, AGU*, *79*(47), 579.
- Whittaker, J., Goncharov, A., Williams, S., Müller, R. D., & Leitchenkov, G. (2013). Global sediment thickness dataset updated for the Australian-Antarctic Southern Ocean. *Geochemistry, Geophysics, Geosystems*, *14*, 3297–3305. doi:10.1002/ggge.20181.
- Wild-Pfeiffer, F. (2008). A comparison of different mass element for use in gravity gradiometry. *Journal of Geodesy*, *82*, 637–653. doi:10.1007/s00190-008-0219-8.
- Yáñez, G. A., Ranero, C. R., von Huene, R., & Diaz, J. (2001). Magnetic anomaly interpretation across the southern Central Andes (32–34 S). The role of the Juan Fernandez Ridge in the late Tertiary evolution of the margin. *Journal of Geophysical Research: Solid Earth*, *106*(B4), 6325–6345.
- Yáñez, G., Cembrano, J., Pardo, M., Ranero, C., & Selles, D. (2002). The Challenger-Juan Fernandez-Maipo major tectonic transition of the Nazca-Andean subduction system at 33–34°S: geodynamic evidence and implications. *Journal of South American Earth Sciences*, *15*, 22–38.

(Received November 25, 2015, revised August 2, 2016, accepted August 5, 2016, Published online August 12, 2016)